Monthly Notices of the ROYAL ASTRONOMICAL SOCIETY

MNRAS **496,** 4606–4623 (2020) doi:10.1093/mnras/staa1811
Advance Access publication 2020 June 23

A panchromatic spatially resolved analysis of nearby galaxies – II. The main sequence – gas relation at sub-kpc scale in grand-design spirals

L. Morselli [1,2]★ G. Rodighiero,[1,2] A. Enia [1,2] E. Corbelli,[3] V. Casasola,[3,4] L. Rodríguez-Muñoz [1] A. Renzini [2] S. Tacchella [5] I. Baronchelli,[3] S. Bianchi [3] P. Cassata,[1,2] A. Franceschini,[1] C. Mancini [1,2] M. Negrello,[6] P. Popesso[7] and M. Romano [1,2]

[1]*Dipartimento di Fisica e Astronomia, Università di Padova, vicolo dell'Osservatorio 3, I-35122 Padova, Italy*
[2]*INAF – Osservatorio Astrofisico di Padova, vicolo dell'Osservatorio 5, I-35122 Padova, Italy*
[3]*INAF – Osservatorio Astrofisico di Arcetri, Largo E. Fermi 5, I-50125, Firenze, Italy*
[4]*INAF – Istituto di Radioastronomia, Via P. Gobetti 101, I-40129, Bologna, Italy*
[5]*Center for Astrophysics | Harvard & Smithsonian, 60 Garden Str, Cambridge, MA 02138, USA*
[6]*School of Physics and Astronomy, Cardiff University, The Parade, Cardiff CF24 3AA, UK*
[7]*Excellence Cluster Universe, Boltzmann strasse 2, D-85748 Garching bei München, Germany*

Accepted 2020 June 18. Received 2020 June 16; in original form 2020 March 5

ABSTRACT

In this work, we analyse the connection between gas availability and the position of a region with respect to the spatially resolved main-sequence (MS) relation. Following the procedure presented in Enia et al. (2020), for a sample of five face-on, grand design spiral galaxies located on the MS we obtain estimates of stellar mass and star formation rate surface densities ($\Sigma_\star$ and $\Sigma_{\rm SFR}$) within cells of 500 pc size. Thanks to H I 21cm and ^{12}CO(2–1) maps of comparable resolution, within the same cells we estimate the surface densities of the atomic ($\Sigma_{\rm H\,I}$) and molecular ($\Sigma_{\rm H_2}$) gas and explore the correlations among all these quantities. $\Sigma_\star$, $\Sigma_{\rm SFR}$, and $\Sigma_{\rm H_2}$ define a 3D relation whose projections are the spatially resolved MS, the Kennicutt–Schmidt law and the molecular gas MS. We find that $\Sigma_{\rm H_2}$ steadily increases along the MS relation and is almost constant perpendicular to it. $\Sigma_{\rm H\,I}$ is nearly constant along the MS and increases in its upper envelope. As a result, $\Sigma_{\rm SFR}$ can be expressed as a function of $\Sigma_\star$ and $\Sigma_{\rm H\,I}$, following the relation $\log \Sigma_{\rm SFR} = 0.97 \log \Sigma_\star + 1.99 \log \Sigma_{\rm H\,I} - 11.11$. We show that the total gas fraction significantly increases towards the starburst regions, accompanied by a weak increase in star formation efficiency. Finally, we find that $\rm H_2/H\,I$ varies strongly with the distance from the MS, dropping dramatically in regions of intense star formation, where the UV radiation from newly formed stars dissociates the $\rm H_2$ molecule, illustrating the self-regulating nature of the star formation process.

Key words: galaxies: evolution – galaxies: star formation – galaxies: spirals.

1 INTRODUCTION

In the current model of galaxy formation and evolution, stars form in dense clouds of molecular gas, thanks to the interplay of different physical mechanisms (magnetic fields, turbulence, shielding, feedback). Despite its complexity, this interplay translates in tight correlations between different physical quantities: (i) between the surface density of the star formation rate ($\Sigma_{\rm SFR}$) and the surface density of the gas ($\Sigma_{\rm gas}$), and (ii) between the stellar mass surface density ($\Sigma_\star$) and $\Sigma_{\rm SFR}$. The first relation, originally formulated by Schmidt (1959) using the gas volume density and the number of stars formed in the solar neighbourhood, was subsequently derived by Kennicutt (1998) for radially averaged surface densities in external galaxies, and it is thus called the Kennicutt–Schmidt (KS) relation. The second, called main sequence (MS), was initially found using integrated quantities of star-forming galaxies (thus the total SFR and stellar mass $M_\star$) in Brinchmann et al. (2004) for local galaxies and later confirmed for high-redshift galaxies by several works (e.g. Daddi et al. 2007; Elbaz et al. 2007; Noeske et al. 2007; Salim et al. 2007). As both relations are intrinsically related to the process of star formation and thus to galaxy evolution as a whole, and because they are fundamental ingredients of theoretical models and simulations, they have been intensively studied in the past (e.g. Tan 2000; Boissier et al. 2003; Springel & Hernquist 2003; Krumholz & McKee 2005; Rodighiero et al. 2011; Kennicutt & Evans 2012; Krumholz, Dekel & McKee 2012; Whitaker et al. 2012; Kashino et al. 2013; Hopkins et al. 2014; Speagle et al. 2014; Genzel et al. 2015; Schreiber et al. 2015; Kurczynski et al. 2016; Tacchella et al. 2016; Santini et al. 2017; Orr et al. 2018; Pearson et al. 2018; Morselli et al. 2019; Popesso et al. 2019).

The KS law relates the fuel of star formation to its end product, stars; its shape has important effects on the depletion time of the gas ($t_{\rm depl} = M_{\rm gas}/{\rm SFR}$, with $M_{\rm gas}$ the total gas mass), or equivalently on the efficiency of the star formation process (${\rm SFE} = {t_{\rm depl}}^{-1} = {\rm SFR}/M_{\rm gas}$). In one of the earliest works, Kennicutt (1998) finds a super-linear correlation (slope = 1.4–1.5) between the total gas and the SFR surface densities. Following this result, several papers investigate the relation between star formation and gas availability, considering different gas phases and star formation tracers, as well as exploring this

★ E-mail: laura.morselli@unipd.it

link at different cosmic epochs (e.g. Wyder et al. 2009; Genzel et al. 2010; Tacconi et al. 2010; Genzel et al. 2012). Bigiel et al. (2008), Leroy et al. (2008), Leroy et al. (2013), and Schruba et al. (2011) exploit molecular and neutral gas observations of nearby galaxies to investigate how the relation between gas and star formation activity varies within galaxies and as a function of local and integrated properties. Overall, their findings indicate that the connection between star formation and molecular gas is a linear relation (i.e. slope $\sim$1), thus implying a constant molecular SFE and $t_{\rm depl}$ (around 2.2 Gyr). Leroy et al. (2013) find second-order variations in the molecular gas $t_{\rm depl}$ and study how some of them can be related to variations in the $\alpha_{\rm CO}$ conversion factor between CO luminosity and H_2 mass, while further variability might arise as a consequence of galaxy properties. Bigiel et al. (2010), instead, study the relation between recent SF activity and H I outside the optical disc, in regions where H I represents the totality of the ISM, and find significant spatial correlation between FUV (tracing recent dust-unobscured star formation) and H I density. They also find that the SFE ($t_{\rm depl}$) decreases (increases) with increasing radius. Similarly, Roychowdhury et al. (2015) study the spatially resolved KS relation on sub-kpc and kpc scales in the H I-dominated regions of nearby spirals and irregular galaxies and find that gas consumption time-scales are longer compared to H_2-dominated regions (lower SFE). Other works investigated, at earlier cosmic epoch, the spatially resolved (e.g. Freundlich et al. 2013; Genzel et al. 2013) and integrated (Freundlich et al. 2019) KS relation. In particular, Freundlich et al. (2019) obtain a linear galaxy-averaged molecular KS relation, implying that galaxies at different cosmic epochs have similar star formation time-scales. This is consistent with the results of Peng & Renzini (2020), which find that the sSFR (SFR/$M_\star$) and $M_{\rm H_2}/M_\star$ have the same redshift evolution, thus implying a linear KS law. On the other hand, galaxy-to-galaxy variations in the molecular gas–star formation relation have also been reported. For example, Ford et al. (2013), Shetty, Kelly & Bigiel (2013), Shetty, Clark & Klessen (2014b), and Shetty et al. (2014a) find evidence for a sub-linear relation within galaxies and for the combined samples. Also, Casasola et al. (2015) find galaxy-to-galaxy variations of the spatially resolved KS relation, and underline that the slope can be both sub-linear and super-linear, depending on the spatial scale. de los Reyes & Kennicutt (2019) revisit the integrated KS law in local, normal star-forming galaxies and find that spirals lie on a tight log-linear relation with slope 1.41 ± 0.07 (when considering both the neutral and molecular gas) while dwarfs populate the region below it.

The second fundamental relation, the MS, relates stars that have already formed to the ongoing SFR. The existence of the MS up to $z \sim 4$ (characterized by a non-evolving slope and scatter and an increasing normalization with increasing redshift, e.g. Speagle et al. 2014; Popesso et al. 2019) was interpreted in the framework of gas-regulated galaxy evolution, according to which galaxies grow along the MS thanks to the continuous replenishment of their gas supply (e.g. Dekel et al. 2009; Bouché et al. 2010; Lilly et al. 2013). The observation of outliers located above the MS relation (starburst are generally classified in literature as galaxies having an SFR that is a factor of 4 higher that the MS value at fixed stellar mass, e.g. Rodighiero et al. 2011) at different cosmic epochs sparkled the interest on whether these sources: (i) have larger gas reservoirs [thus a higher gas fraction, $f_{\rm gas} = M_{\rm gas}/(M_{\rm gas} + M_\star)$, e.g. Lee et al. 2017], (ii) are more efficient in converting gas into stars (thus a higher SFE, e.g. Solomon et al. 1997; Daddi et al. 2010; Silverman et al. 2015, 2018; Ellison et al. 2020a), or (iii) a combination of both (e.g. Saintonge et al. 2011a, 2012; Huang & Kauffmann 2014; Scoville et al. 2017; Tacconi et al. 2018). In the recent years, the advent of large integral field spectroscopic (IFS) surveys revealed that the integrated MS relation originates at smaller scales (up to the sizes of molecular clouds), thus implying that the star formation process is regulated by physical process that act on sub-galactic scales (Cano-Díaz et al. 2016; Abdurro'uf & Akiyama 2017; Hsieh et al. 2017; Lin et al. 2017; Hall et al. 2018; Medling et al. 2018; Cano-Díaz et al. 2019; Vulcani et al. 2019; Bluck et al. 2020; Enia et al. 2020). Despite a general consensus on the existence of the spatially resolved MS, the slope, intercept, and scatter of the relation vary significantly among different works, depending on the sample selection, SFR indicator, dust correction, and fitting procedure. Moreover, some authors find that the spatially resolved relation vary dramatically from galaxy to galaxy. Recently, the combination of MaNGA (Mapping Nearby Galaxies at APO, Bundy et al. 2015) and ALMaQUEST (the ALMA-MaNGA QUEnching and STar formation survey) allowed the study of the link between the spatially resolved MS and gas reservoirs and the investigation of the nature of starburst regions within galaxies. By analysing 14 MS galaxies, Lin et al. (2019) suggest that the MS relation originates from two more fundamental relations: the molecular KS and the so-called MGMS, a relation between $\Sigma_\star$ and $\Sigma_{\rm H2}$. Ellison et al. (2020b) exploit 34 galaxies in ALMaQUEST to study the nature of variations in the SFR on kpc scales. They find that while the average SFR is regulated by the availability of molecular gas, the scatter of the spatially resolved MS (and thus variations with respect to the average SFR value) originates in variations of the SFE. Dey et al. (2019), using optical IFU and CO observations collected in the EDGE-CALIFA survey (CARMA Extragalactic Database for Galaxy Evolution Bolatto et al. 2017, see also Barrera-Ballesteros et al. 2020), find that $\Sigma_{\rm SFR}$ is a function of both $\Sigma_\star$ and $\Sigma_{\rm H_2}$, but different from Lin et al. (2019), the relation with the stellar mass is statistically more significant than the one with the molecular gas. Early works on the formation of molecular hydrogen in the ISM, such as Elmegreen (1993) and Blitz & Rosolowsky (2006), have underlined the role of the disc hydrostatic pressure, and hence of $\Sigma_\star$, in promoting the formation of molecules. Also the works of Shi et al. (2011) and Shi et al. (2018), that propose an *extended KS law* expressed as a proportionality between Σ_{SFE} and $\Sigma_\star$, emphasize the role of existing stars in setting the current production of stars, which indeed is the very nature of the MS.

In this paper, we build on the work presented in Enia et al. (2020, hereafter Paper I) and analyse the sub-kpc relation between the surface densities of star formation, gas in different phases, and stellar mass in five local grand-design spirals. In Paper I, we exploit multiwavelength observations in more than 20 photometric bands to obtain spatially resolved estimates of $\Sigma_\star$ and $\Sigma_{\rm SFR}$ on different physical scales, from few hundred parsecs to 1.5 kpc, via SED fitting. We use these estimates to study the spatially resolved MS relation and find the slope to be consistent for different spatial scales, as well as with the slope of the integrated relation. Here, we aim at analysing under which gas properties different spatial regions populate different loci of the spatially resolved MS, thus trying to understand whether the SFR is more connected to the gravity of the disc (dominated by stars up to $\sim$2/3 of the optical radius) or with the availability of fuel, or a combination of both. We exploit observations in more than 20 photometric bands to derive accurate SFR and $M_\star$ maps to compare to H I and H_2 maps. We discuss the origin of the spatially resolved MS, in terms of its slope and scatter.

The structure of the paper is the following. In Section 2, we give a short description of the data used in this work; in Section 3, we present our results at 500 pc resolution; in Section 4, we analyse the implications of our results on the existence of the MS relation and

Table 1. Properties of the galaxies in our sample: (1) galaxy name; (2,3) RA and Dec coordinates in J2000; (4) total $M_\star$ from SED fitting; (5) total SFR computed from equation (1) with L_{UV} and L_{IR} from SED fitting; (6,7) distance in Mpc and radius in kpc at which the optical surface brightness falls below 25 mag arcsec^{-2}, both taken from the HyperLEDA data base; (8) total H I mass in R_{25}; (9) total H_2 mass in R_{25}; (10) morphological T type, taken from HyperLEDA; (11) central metallicity computed using the O3N2 index, and taken from the DustPedia archive.

Galaxy name	RA (deg)	Dec. (deg)	log$M_\star$ ($M_\odot$)	SFR ($M_\odot$ yr^{-1})	D (Mpc)	R_{25} (kpc)	log$M_{H\,I}$ ($M_\odot$)	logM_{H_2} ($M_\odot$)	T	12 + log(O/H)
NGC 0628 (M74)	24.174	15.7833	10.31 ± 0.15	1.78 ± 0.41	10.14	14.74	9.54 ± 0.18	9.39 ± 0.20	5.2	8.693 ± 0.001
NGC 3184	154.5708	41.4244	10.13 ± 0.10	1.02 ± 0.10	11.64	12.55	9.38 ± 0.14	9.20 ± 0.24	5.9	$8.766^{+0.014}_{-0.013}$
NGC 5194 (M51a)	202.8025	47.1952	10.74 ± 0.20	3.68 ± 0.26	8.59	17.23	9.43 ± 0.17	9.86 ± 0.22	4.0	$8.824^{+0.017}_{-0.016}$
NGC 5457 (M101)	210.8025	54.3491	10.37 ± 0.13	3.00 ± 0.15	7.11	24.81	10.15 ± 0.14	9.41 ± 0.18	5.9	$8.528^{+0.006}_{-0.007}$
NGC 6946	308.71905	60.15361	10.61 ± 0.13	3.51 ± 0.15	6.73	24.81	9.41 ± 0.15	9.74 ± 0.17	5.9	$8.746^{+0.067}_{-0.070}$

on how SFE and f_{gas} vary with varying SFR. Finally, in Section 5 we summarize our findings. The assumed IMF is Chabrier (2003), cosmology is ΛCDM with parameters from Planck Collaboration XIII (2016).

2 DATA

This work is based on multiwavelength observations of five nearby face-on spiral galaxies: NGC 0628, NGC 3184, NGC 5194, NGC 5457, and NGC 6946. Four out of five galaxies are in common with Paper I: they are the ones observed in 23 photometric bands, and included in the THINGS and HERACLES surveys. NGC 6946 was initially excluded from the Paper I sample, since it lacked optical observations (the five Sloan optical filters). We tested for the sample in Paper I how the SED fitting routine results change excluding these five photometric points, finding that they are nearly unchanged. Following this, we are including NGC 6946 in this analysis. The observations in 23 different bands (18 for NGC 6946) have been collected in the DustPedia [1] (Davies et al. 2017; Clark et al. 2018) archive; more details on the data set can be found in Paper I and references therein. The main properties of the galaxies in this sample are shown in Table 1. We highlight two properties of our sample: (i) according to the integrated SFR and $M_\star$ values, the objects in our sample are MS galaxies, located within 0.2 dex from the relation obtained in Paper I, and (ii) three out of five sources are classified as SAB spirals (NGC 3184, NGC 5457, and NGC 6946), thus show evidence of a bar component.

2.1 SFRs, stellar mass, and distance from the MS

The spatially resolved measurements at 500 pc resolution of $\Sigma_\star$, Σ_{SFR}, and distance from the MS (Δ_{MS}), have been obtained following the procedure presented in Paper I. Briefly, we select 8 nearby, face-on, grand design spiral MS galaxies with log $M_\star \sim$ 10.4–10.6 $M_\odot$, and perform spatially resolved SED fitting to 23 photometric bands using MAGPHYS (da Cunha, Charlot & Elbaz 2008). In particular, we performed SED fitting on cells having two different side measurements: 8 arcsec (thus a varying physical scale between 290 and 700 pc, depending on the distance of the galaxies) and 1.5 kpc. Here, we implement an improved procedure and performed SED fitting at a common resolution of 500 pc (as discussed in Paper I, these scales are higher than the ones where the energy-balance criterion holds, ∼200–400 pc). The procedural improvements are the following: (i) we estimate the noise on the photometry of each cell from the rms maps (while in Paper I we used the DustPedia photometry signal-to-noise ratio); (ii) if a cell has more than 10 bands with SNR < 2 it is automatically excluded from the SED fitting procedure, thus reducing computational time. These improvements influence the χ^2 estimation in MAGPHYS, increasing the number of accepted points within the optical radius, and leading to cleaner results in the outer part of galaxies, where the photometry is fainter. The slope and intercept of the spatially resolved MS given in Paper I do not change when these improvements are implemented in the pipeline.

In each cell, the SFR is computed as the sum of unobscured (SFR_{UV}) and obscured (SFR_{IR}) star formation activity, obtained using the relations of Bell & Kennicutt (2001) and Kennicutt (1998) (reported to Chabrier IMF):

$$SFR = 0.88 \times 10^{-28} L_{UV} + 2.64 \times 10^{-44} L_{IR}, \quad (1)$$

where L_{UV} and L_{IR} are taken from the best-fitting SED and are the luminosity (in erg s^{-1} Hz^{-1}) at 150 nm and the one (in erg s^{-1}) integrated between 8 and 1000 μm, respectively. As shown in fig. 3 of Paper I, the SFR computed following equation (1) and the one that MAGPHYS gives as output are highly consistent. Here, for consistency with Paper I, we use the SFRs estimated with equation (1), but the results would not change when considering the SFRs given as output of the SED-fitting procedure.

As the sample of galaxies used here differs from the one of Paper I, we decided to recompute the spatially resolved MS for this sample, but following the same procedure, i.e. (1) by fitting with a log-linear relation the median values of logΣ_{SFR} in bins of log$\Sigma_\star$, using EMCEE (Foreman-Mackey et al. 2013) and considering 10 bins in the log$\Sigma_\star$ range [6.5:8.5] $M_\odot$ pc^{-2}, plus an additional bin to include the few points between [8.5:9.5] $M_\odot$ pc^{-2}, and (2) by implementing an orthogonal distance regression (ODR) technique. The slope and intercept of the MS are 0.76(±0.20) and −8.15(±1.63) with the first method, and 0.87(±0.01) and −8.94(±0.06) with the second. These estimates are consistent with the ones in Paper I. In the following analysis we make use of the distance from the MS relation computed with the binning technique, but our results do not change when considering the ODR MS relation.

For each region, we compute the distance from the MS as the difference between log Σ_{SFR} and the MS value (in log) estimated for the $\Sigma_\star$ of the region, thus Δ_{MS} = log Σ_{SFR} − (0.76log $\Sigma_\star$ − 8.15). The left-hand panel of Fig. 1 shows, as an example, the Δ_{MS} map of NGC 0628; cells in red are located below the spatially resolved MS, while the ones in blue are located above the relation (the Δ_{MS} maps of the other galaxies in the sample are shown in Appendix B). Within the optical radius (the dashed circle), we are able to recover most of

[1]The DustPedia data base is available at http://DustPedia.astro.noa.gr.

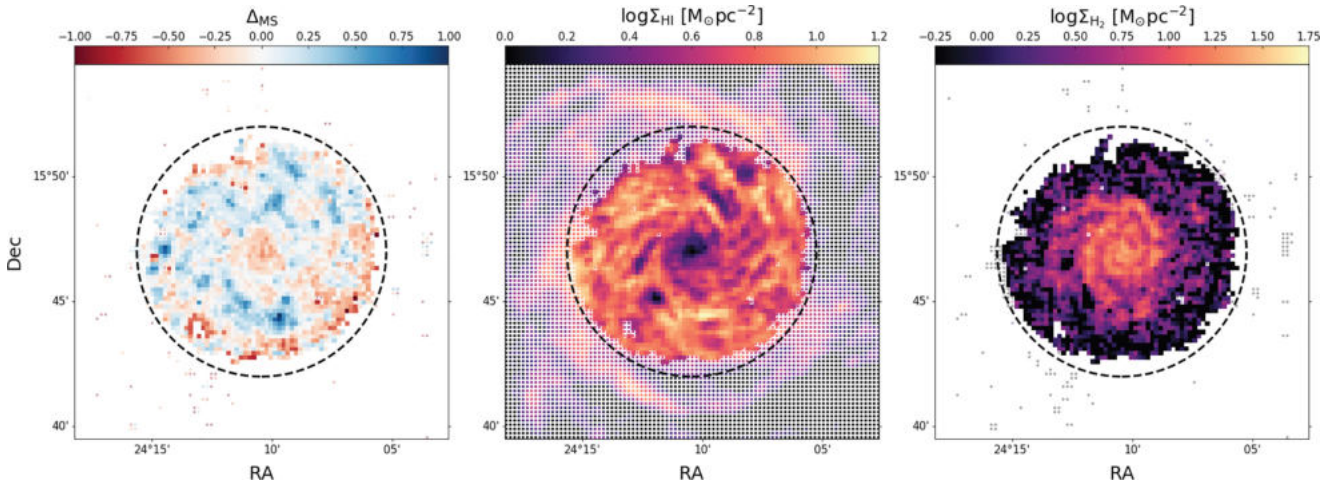

Figure 1. Spatially resolved properties of NGC 0628: Δ_{MS} in the *left-hand panel*, $\log \Sigma_{H\,I}$ in the *central panel*, and $\log \Sigma_{H_2}$ in the *right-hand panel*. The dashed circle has a radius equal to the optical radius of the galaxy, R_{25}. In the left-hand and right-hand panels, small dots are the cells where the SED fitting is characterized by a large χ^2 and are thus rejected. In the central panel, the dotted points are the ones with measured $\log \Sigma_{H\,I}$ but no (or rejected) Δ_{MS}.

the cells, especially at $r < 0.9\ R_{25}$.[2] We emphasize here that the MS relation we obtain is well defined also in the outer parts of the optical disc, where the SFR and $M_\star$ are small in absolute values. We refer the reader to Paper I for details on the SED-fitting procedure, as well as for how the spatially resolved MS relation is obtained.

2.2 Neutral gas: H I 21 cm observations

Neutral hydrogen mass surface densities ($\Sigma_{H\,I}$) are measured from 21cm maps available from the THINGS survey (The H I Nearby Galaxy Survey; Walter et al. 2008). These observations have been carried out with the Very Large Array (VLA) and are characterized by a high angular resolution (6 arcsec and 10 arcsec in the robust and natural weighting, respectively). To compute the H I surface brightness, $\Sigma_{H\,I}$, we first convolve the 21 cm natural-weighted intensity maps, given in Jy beam^{-1} m s^{-1}, to the resolution of the worst of the 23 photometric bands used in the SED fitting (the one of SPIRE350, 24 arcsec, see Paper I) using a Gaussian kernel. We used the beam sizes given in table 2 of Walter et al. (2008) and equation 1 to obtain the flux in K km s^{-1} and then estimate $\Sigma_{H\,I}$ from equation 5 of Walter et al. (2008) (that does not include a correction for helium). We compute the sensitivity limit from our maps of $\Sigma_{H\,I}$ at 500 pc resolution and find $\Sigma_{H\,I,lim} \sim 2$ M$_\odot$ pc^{-2}. The central panel of Fig. 1 shows the distribution of $\Sigma_{H\,I}$ in NGC 0628. As in several other spiral galaxies, the H I is centrally depressed (e.g. Casasola et al. 2017), and it extends on radius that are significantly larger that the optical radius (Swaters et al. 2002; Wang et al. 2013). The values of $M_{H\,I}$ within R_{25} are reported in Table 1. For the galaxies in our sample, the H I gas-to-stellar mass ratio ($M_{H\,I}/M_\star$) within R_{25} varies from 5 per cent to 60 per cent.

2.3 Molecular gas: CO observations

The molecular gas surface density, Σ_{H_2}, is computed using the ^{12}CO(2−1) intensity maps from the HERACLES survey (The HERA CO-Line Extragalactic Survey; Leroy et al. 2009). These observations were made with the IRAM 30 m telescope and have an angular resolution of 11 arcsec. As for $\Sigma_{H\,I}$, we convolve the images using a Gaussian kernel to the resolution of SPIRE350. We estimated Σ_{H_2} using equation 4 of Leroy et al. (2009), considering a metallicity independent conversion factor X_{CO} ($X_{CO} = N(H_2)/I_{CO}$, where $N(H_2)$ is the H_2 column density and I_{CO} is the line intensity) equal to 2×10^{20} cm^{-2}(K km s^{-1})$^{-1}$ (the typical value for disc galaxies, see e.g. Bolatto, Wolfire & Leroy 2013), and a CO line ratio $I_{CO(2-1)}/I_{CO(1-0)} = 0.8$ (e.g. Leroy et al. 2009; Schruba et al. 2011; Casasola et al. 2015). We divide by a factor of 1.36 that is included in equation 4 of Leroy et al. (2009) to remove the helium contribution. In Section 3 we show that the results presented here remain true when considering a metallicity-dependent X_{CO} factor, using the X_{CO}−(12 + log O/H) relation of Genzel et al. (2011) and the spatially resolved metallicity measurements collected in DustPedia. The sensitivity limit, computed as the rms of our $\log\Sigma_{H_2}$ maps at 500 pc resolution, is $\log\Sigma_{H_2,\,lim} = 0.4$ M$_\odot$ pc^{-2}. For the regions corresponding to a negative flux of ^{12}CO(2 − 1), in the $\Sigma_{H_2,\,lim}$ map we replace the value with a randomly generated number between 0 and the sensitivity limit, so that Σ_{H_2} can be computed as an upper limit. While this step does not influence our results concerning H_2, it allows us to extend the analysis also to the regions where H_2 is not detected. The right-hand panel of Fig. 1 shows the distribution of Σ_{H_2} in NGC 0628. The H_2 is centrally concentrated, and mostly below the sensitivity limit for $r > 0.5R_{25}$. For the galaxies in our sample, the H_2 gas-to-stellar mass ratio ($M_{H_2}/M_\star$) within R_{25} is almost constant around 11–14 per cent.

3 RESULTS

Before analysing the spatially resolved connection between star formation and gas components, we briefly comment on the integrated properties of the galaxies in our sample. It is worth underlying that, within R_{25}, three out of five galaxies have similar amount of neutral and molecular gas (M_{H_2} and $M_{H\,I}$), within the uncertainties. This is consistent with the results of Casasola et al. (2020), as they find that, within R_{25}, galaxies with morphological type $T = 4, 5, 6$ have $M_{H_2}/M_{H\,I} = 0.91$, 1, and 1.05, respectively. For NGC 5457 and NGC

[2] R_{25} is defined as the length of the projected semimajor axis of a galaxy at the isophotal level 25 mag arcsec^{-2} in the *B* band and it is taken from the HyperLEDA data base (Makarov et al. 2014).

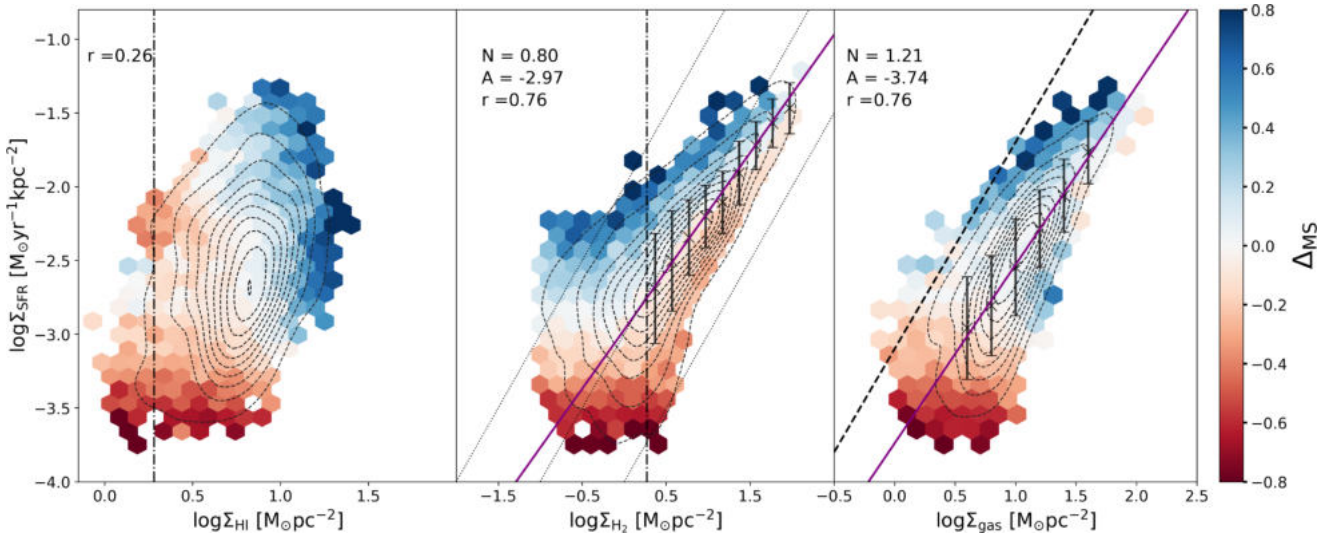

Figure 2. Relations between Σ_{SFR} and $\Sigma_{H\,I}$ (left-hand panel), Σ_{H_2} (middle panel), and Σ_{gas} (for the total H I+H_2 gas, right-hand panel) colour coded as a function of the median value of Δ_{MS} in each bin. Only bins containing a minimum number of three cells are shown in the plot. The dashed contours encircle the areas of the plane containing from 10 per cent to 90 per cent of the data, at steps of 10 per cent. The sensitivity limits are represented by the dot–dashed black lines. The purple solid lines in the middle and right-hand panel represent the best fit to the data obtained fitting the points marked with crosses; the corresponding slope (*N*) and intercept (*A*) are written in the panels, together with the Spearman correlation coefficient *r*.
In the central panel, the dotted lines mark constant molecular t_{depl} of 10^8, 10^9, and 10^{10} yr from top to bottom. In the right-hand panel, the dashed black line is the fit to local ULIRGs and SMGs taken from Daddi et al. (2010).

5194, the average value associated with their morphological type does not describe well their gas properties. It is well know that NGC 5457 is likely to have experienced a recent event of gas accretion (Mihos et al. 2013; Vílchez et al. 2019) which can explain the H I rich outer disc and its high total H I mass. A high molecular gas mass fraction, as for NGC 5194, is likely the result of tidal stirring by a companion.

3.1 Dependency of the SFR on gas

With the data set in our hands, we first investigate the spatially resolved relations between the SFR and the different gas phases, by analysing how Σ_{SFR} relates to $\Sigma_{H\,I}$, Σ_{H_2}, and Σ_{gas}. This last quantity is computed as the sum of the neutral and molecular component for all the regions where the Σ_{H_2} is above the sensitivity limit, while it is equal to Σ_{H_I} otherwise, and it is thus a lower limit. The results of this exercise are shown in Fig. 2.

As expected, no significant correlation is found between Σ_{SFR} and $\Sigma_{H\,I}$ (Spearman correlation coefficient $r = 0.26$), while tight correlations are present between Σ_{SFR} and Σ_{H_2}, and Σ_{SFR} and Σ_{gas} ($r = 0.76$), confirming several results in the literature (e.g. Bigiel et al. 2008; Kumari, Irwin & James 2020). In Fig. 2, we add the information on how regions located at different distance from the spatially resolved MS populate the $\log\Sigma_{SFR} - \log\Sigma_{H\,I/H_2/gas}$ plane. To do so, we divide the $\log\Sigma_{SFR}$–$\log\Sigma_{H\,I/H_2/gas}$ planes in bins colour coded according to the median value of Δ_{MS} in each bin. We observe that regions above the MS are found in correspondence to the highest $\Sigma_{H\,I}$, but span a wide range of Σ_{H_2} values. Analogously, regions located below the MS are preferentially found at lower $\Sigma_{H\,I}$, while are characterized by Σ_{H_2} spanning the whole range of possible values. For $\log\Sigma_{SFR} > -2$, the trend between $\log\Sigma_{H\,I}$ and Δ_{MS} is less evident; this is due to the fact that we are not well sampling the region below the MS, as shown in fig. 5 of Paper I, and confirmed by the decrease of the scatter of the spatially resolved MS at the higher stellar surface densities. Analogously, the points with $\log\Sigma_{SFR} < -3$ are mostly found on the MS or below it, thus hiding a possible trend at the lowest SFRs. When considering the total gas, we see that regions closer to the relation that describes local Ultra-Luminous IR Galaxies (ULIRGs) and sub-mm galaxies (dashed black lines, taken from Daddi et al. 2010) are the ones located above the relation. On the other hand, the general behaviour between the distance from the best-fitting relation and the distance from the MS is less regular than in the case of molecular gas. Indeed, the central panel of Fig. 2 suggests that the spatially resolved MS is intrinsically linked to the molecular gas–SFR relation, as MS regions (in white) fall very consistently along the $\log\Sigma_{SFR}$–$\log\Sigma_{H_2}$ relation. Regions that populate the upper (lower) envelope of the molecular KS law are also found in the upper (lower) envelope of the spatially resolved MS relation. This is qualitatively consistent with what found by Ellison et al. (2020b) when analysing the molecular gas–SFR relation exploiting ALMA and MaNGA data on kpc scales.

By fitting the average values of $\log\Sigma_{SFR}$ in bins of $\log\Sigma_{H_2}$ and $\log\Sigma_{gas}$ (both above the sensitivity limit of $\log\Sigma_{H_2}$), we find the following scaling relations (slopes *N* and intercepts *A* are also written in the corresponding panels):

$$\log \Sigma_{SFR} = 0.80(\pm0.12) \times \log \Sigma_{H_2} - 2.97(\pm0.85) \quad (2)$$

and

$$\log \Sigma_{SFR} = 1.21(\pm0.18) \times \log \Sigma_{gas} - 3.74(\pm1.15) \quad (3)$$

The two correlations have equal strength according to the Spearman coefficient, and their scatter is in both cases smaller than the one of the spatially resolved MS: 0.19 for the $\log\Sigma_{H_2}$–$\log\Sigma_{SFR}$ relation and 0.17 for the $\log\Sigma_{gas}$–$\log\Sigma_{SFR}$. The relation between $\log\Sigma_{SFR}$ and $\log\Sigma_{H_2}$ is sub-linear, but becomes linear when the ODR fitting is applied. We retrieve a molecular t_{depl} that varies between 1.6 and 3 Gyr. These results are in agreement with the typical t_{depl} in normal spiral galaxies (see e.g. Bigiel et al. 2008; Saintonge et al. 2011b; Leroy et al. 2013; Casasola et al. 2015). It is worth noticing that the slope of the spatially resolved KS relation obtained from

Table 2. Slope, intercept, and scatter of the following relations: molecular KS law, log Σ_{gas}–log Σ_{SFR}, MGMS, and log $\Sigma_\star$–log Σ_{gas}. We list the best-fitting parameters for log Σ_{H_2} computed using a constant XCO factor and a metallicity dependent XCO obtained from estimates of the metallicity that use (1) the N2 index and (2) the O3N2 index.

Correlation	Slope			Intercept			Scatter		
	Const α_{CO}	O3N2	N2	Const α_{CO}	O3N2	N2	Const α_{CO}	O3N2	N2
log Σ_{H_2}–log Σ_{SFR}	0.80 ± 0.12	0.83 ± 0.12	0.83 ± 0.11	−2.97 ± 0.87	−2.97 ± 0.93	−2.94 ± 0.94	0.19	0.20	0.19
log Σ_{gas}–log Σ_{SFR}	1.21 ± 0.18	1.24 ± 0.16	1.25 ± 0.18	−3.74 ± 1.15	−3.74 ± 1.15	−3.73 ± 1.14	0.17	0.18	0.18
log $\Sigma_\star$–log Σ_{H_2}	0.91 ± 0.29	0.84 ± 0.29	0.87 ± 0.27	−6.15 ± 2.11	−5.66 ± 2.12	−5.93 ± 2.07	0.22	0.24	0.23
log $\Sigma_\star$–log Σ_{gas}	0.50 ± 0.14	0.49 ± 0.14	0.49 ± 0.13	−2.64 ± 0.97	−2.62 ± 1.08	−2.72 ± 1.05	0.24	0.25	0.25

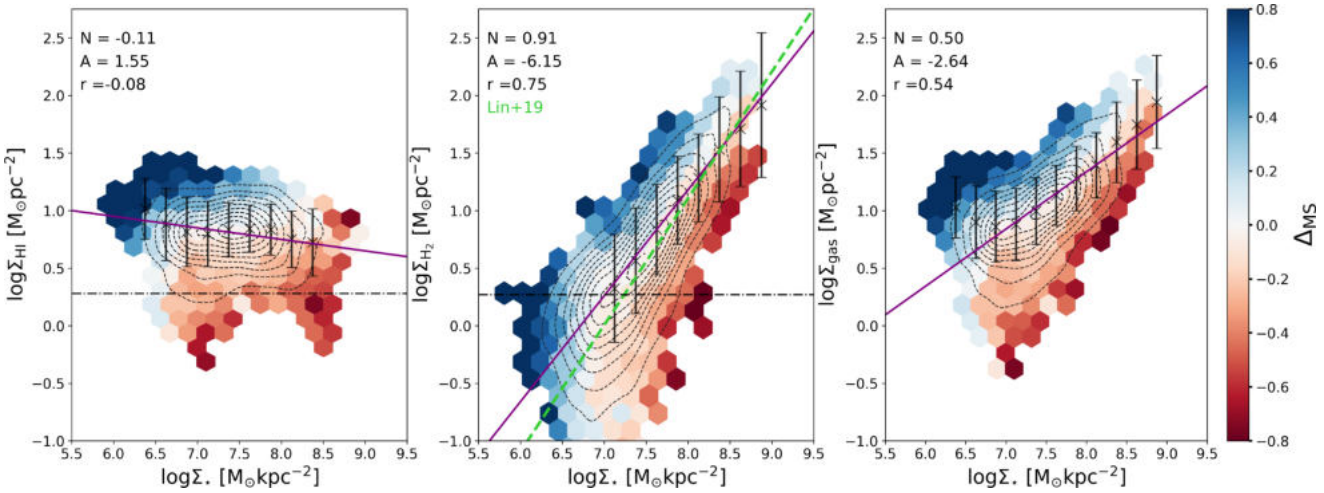

Figure 3. Distributions of the regions in the log $\Sigma_\star$–log $\Sigma_{H\,I}$ plane (left-hand panel), log $\Sigma_\star$–log Σ_{H_2} plane (central panel) and log $\Sigma_\star$–log Σ_{gas} plane (right-hand panel). Each hexagonal bin the plane has been colour coded according to the average value of Δ_{MS}, as in Fig. 2. The purple solid lines are the best-fitting relations obtained by fitting the average values of log$\Sigma_{H\,I,H_2,gas}$ in bins of log $\Sigma_\star$, as marked with black crosses; the slope (N) and intercept (A) of the best fit are written in the panels, together with the Spearman correlation coefficient r. The green dashed line in the central panel is the MGMS of Lin et al. (2019), re-scaled to a Chabrier IMF.

the molecular and total gas are consistent, within errors, with the integrated relations (e.g. Genzel et al. 2010; Kennicutt & Evans 2012; Tacconi et al. 2013; de los Reyes & Kennicutt 2019; Freundlich et al. 2019), similar to what is found when comparing the spatially resolved and integrated MS relation. The scatter of the integrated relation is instead significantly higher (e.g. 0.28 in de los Reyes & Kennicutt 2019).

Finally, we underline here that the trends observed in Fig. 2 are not driven by one or few of the galaxies in our sample, but by and large are common to all five galaxies in our sample. Slope and intercept of the log Σ_{H_2}–log Σ_{SFR} and log Σ_{gas}–log Σ_{SFR} relations are summarized in Table 2.

3.2 Dependence of gas distribution on stellar mass

As the trends shown in Fig. 2 with Δ_{MS} are related to variations of the gas content with $M_\star$, we show in Fig. 3 how the surface densities of neutral, molecular, and total gas vary as a function of $\Sigma_\star$. The left-hand panel of Fig. 3 shows that a very weak anticorrelation is found between log$\Sigma_\star$ and log$\Sigma_{H\,I}$. Indeed, when fitting the average values of log $\Sigma_{H\,I}$ in bins of log $\Sigma_\star$, the slope of the correlation is -0.11 ± 0.07. We stress that every galaxy shows a trend of decreasing $\Sigma_{H\,I}$ towards the central regions, as in the central region the high pressure favours the H I to H_2 transition and most of the gas is in molecular form, but such a decrease can be more or less pronounced from galaxy to galaxy, and does not follow a universal behaviour. Starbursting regions are preferentially located at $r > 0.5R_{25}$, where the surface density of stars falls below 10^7 M⊙ pc^{-2}, and are generally found along the spiral arms.

The relation between log $\Sigma_\star$ and log Σ_{H_2}, shown in the central panel of Fig. 3, is consistently common to all five galaxies and gives birth to a very tight correlation, the MGMS (Lin et al. 2019). The MGMS (re-scaled to a Chabrier IMF) of Lin et al. (2019) is indicated with a green dashed line in the central panel of Fig. 3 and has a slope of 1.1. To obtain the slope of our MGMS relation, we fit the average values of log Σ_{H_2} in bins of log $\Sigma_\star$, restricting the analysis to stellar surface densities where the average value of log Σ_{H_2} is above the sensitivity limit. We find

$$\log \Sigma_{H_2} = 0.91(\pm 0.29) \times \log \Sigma_\star - 6.15(\pm 2.11). \quad (4)$$

This relation has a scatter of 0.22 dex, similar to that obtained for the MS (0.23 dex), and the Spearman coefficient is the same as for the log $\Sigma_{H_2/gas}$–log Σ_{SFR} relations. We find a slope that is consistent within the error with the one of Lin et al. (2019), i.e. 1.1. The different slopes can be ascribed to different fitting procedures; indeed, if we follow the ODR method, we also retrieve a super-linear slope. Regions with the largest sSFR are located in the upper envelope of this relation; in other words, cells located above the spatially resolved MS are also located above the log $\Sigma_\star$–log Σ_{H_2} relation. This trend, outlined also in Ellison et al. (2020b), is here as significant as the one visible in Fig. 2 for the molecular KS relation.

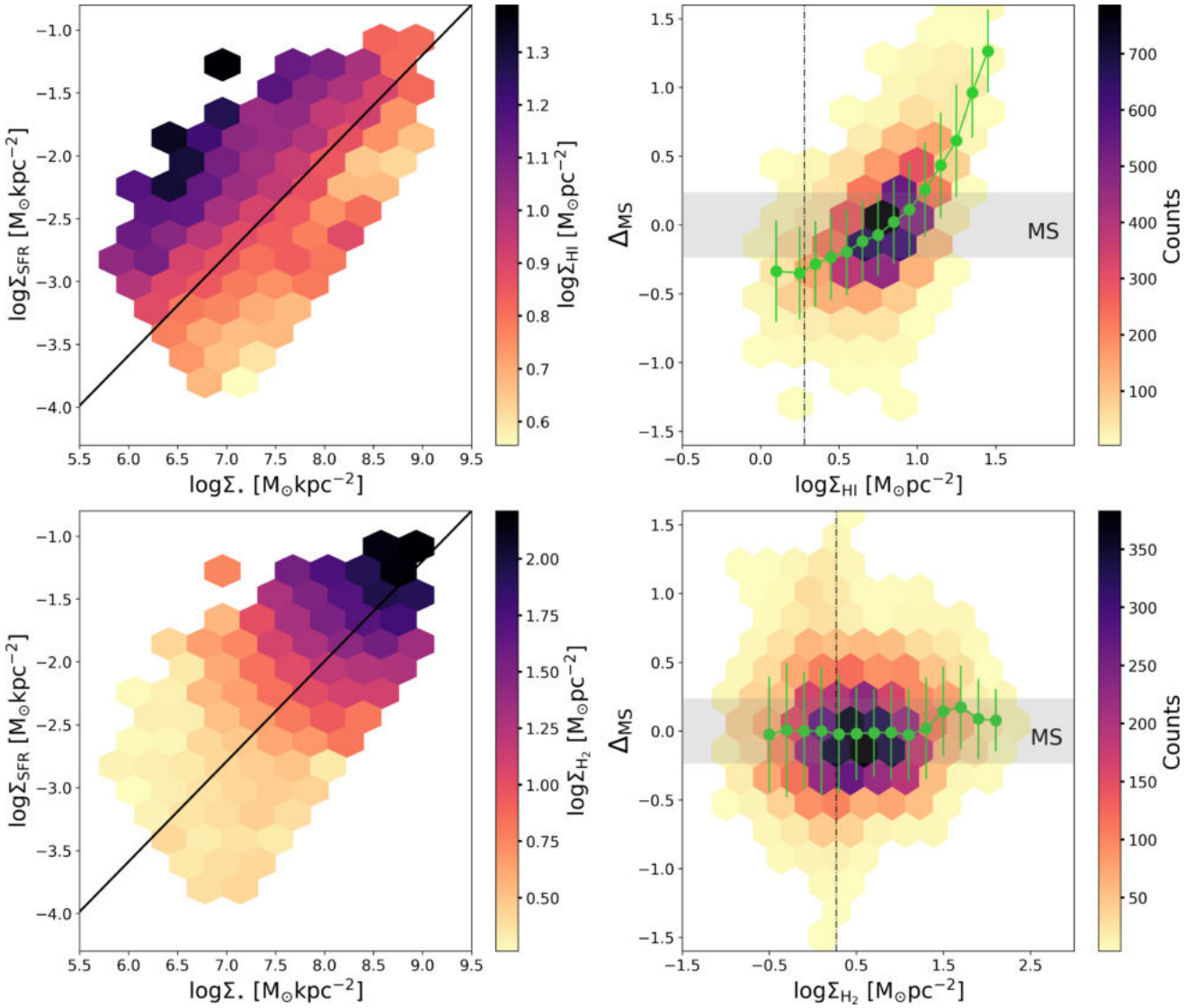

Figure 4. H I and H_2 in the $\log\Sigma_\star$–$\log\Sigma_{SFR}$ plane. Top left-hand panel: $\log\Sigma_\star$–$\log\Sigma_{SFR}$ plane colour coded as a function of the average value of $\log\Sigma_{HI}$ in each bin. The black sold line marks the location of the spatially resolved MS relation. Top right-hand panel: Δ_{MS}, as a function of $\log\Sigma_{HI}$. The average values of Δ_{MS} computed in bins of $\log\Sigma_{HI}$ are shown in green. Each bin is colour coded as a function of the number of cells that it contains. Bottom left-hand panel: $\log\Sigma_\star$–$\log\Sigma_{SFR}$ plane colour coded as a function of the average value of $\log\Sigma_{H_2}$ in each bin. The black sold line marks the location of the spatially resolved MS relation. Bottom right-hand panel: Δ_{MS}, as a function of $\log\Sigma_{H_2}$. The average values of Δ_{MS} computed in bins of $\log\Sigma_{H_2}$ are shown in green. Each bin is colour coded as a function of the number of cells that it contains. In the right-hand panels, the grey shaded area marks the MS region.

A correlation is also apparent between $\log\Sigma_\star$ and $\log\Sigma_{gas}$, that is the combination of the two behaviours seen in the left and central panel of Fig. 3. At low $\Sigma_\star$ ($\log\Sigma_\star \lesssim 7$), the H I tends to dominate over H_2, and the scatter of the relation is larger, while it is slightly narrower at large $\Sigma_\star$. This combined behaviour results in a slope of 0.50 ± 0.14 and an intercept of -2.64 ± 0.97, and a Spearman coefficient of 0.54. Slope and intercept of the $\log\Sigma_\star$–$\log\Sigma_{gas}$ and $\log\Sigma_\star$–$\log\Sigma_{H_2}$ relations are summarized in Table 2.

3.3 H I and H_2 in the $\Sigma_\star$–Σ_{SFR} plane

To further analyse the link between the atomic, molecular, and total gas and the star formation properties of a region, we show in Fig. 4 how $\log\Sigma_{HI}$ and $\log\Sigma_{H_2}$ vary across the $\log\Sigma_\star$–$\log\Sigma_{SFR}$ plane. In the two left-hand panels of Fig. 4, we show the $\log\Sigma_\star$–$\log\Sigma_{SFR}$ plane colour coded as a function of the average $\log\Sigma_{HI}$ (top) and $\log\Sigma_{H_2}$ (bottom) values in each bin. The spatially resolved MS is indicated with the black solid line. To compute the average value of $\log\Sigma_{H_2}$, we also used values below the sensitivity limit; therefore, it is important to emphasize that H_2 is detected only for Σ_{H_2} above $\sim 3\ M_\odot\ pc^{-2}$ that requires a $\Sigma_\star$ higher than $10^7\ M_\odot\ kpc^{-2}$. On the other hand, H_2 column densities below this threshold value are hardly self-shielded and quite rare (e.g. Sternberg et al. 2014).

Interestingly, along the MS relation the average value of $\log\Sigma_{HI}$ is fairly constant and equal to about $7\ M_\odot\ pc^{-2}$ that corresponds to an H I column density of about $9 \times 10^{20}\ cm^{-2}$. This indicates that for cells on the MS, the radiation field is strong enough to partially dissociate H_2, and large amounts of dust-rich H I gas prevent further H_2 dissociation (Sternberg et al. 2014). As expected, Σ_{H_2} increases with increasing $M_\star$, following the MGMS relation, suggesting that the gravity dominated by stars compresses and enhances the ISM

volume density, thus favouring the formation of molecules. The upper envelope of the MS is populated by cells that, on average, have larger H I surface densities than counterparts located on the relation and below it. Focusing on H_2, we can see that no variations in $\log\Sigma_{H_2}$ are visible perpendicular to the MS relation, while a weak trend on increasing $\log\Sigma_{H_2}$ towards higher $\log\Sigma_{SFR}$ can be seen at fixed stellar surface density. For example, at $\log\Sigma_\star = 7.5$ the average value of $\log\Sigma_{H_2}$ on the MS is 0.8 $M_\odot$ pc^{-2}, and increases to $\sim$1.35 $M_\odot$ pc^{-2} 0.8 dex above the relation. Following equation (2), this variation in $\log\Sigma_{H_2}$ would correspond to a difference in $\log\Sigma_{SFR}$ of $\sim$0.5 dex, implying that the increase in H_2 seen at fixed stellar surface densities is not sufficient alone in setting large SFR. In the right-hand panels of Fig. 4, we show the distance from the spatially resolved MS plotted as a function of $\log\Sigma_{H\,I}$ (top) and $\log\Sigma_{H_2}$ (bottom). As indicated qualitatively from Fig. 2, we observe a correlation between $\log\Sigma_{H\,I}$ and Δ_{MS}, for which regions located above the MS are characterized by the largest H I surface brightness, while regions below the MS correspond to cells with low $\log\Sigma_{H\,I}$. We do not observe any correlation between $\log\Sigma_{H_2}$ and Δ_{MS}. This is the combination of the two previous results: (1) the molecular KS relation is populated by regions on the MS and (2) the existence of the MGMS. This suggests that the absolute quantity of molecular gas in a region (or, equivalently its surface density) is not related to the sSFR of the region itself.

3.4 Dependence of the results on metallicity

A possible source of uncertainty in this work is the dependence of the conversion factor between CO and H_2 on gas-phase metallicity (α_{CO}). Indeed, several works have shown that α_{CO} varies strongly as a function of the metallicity (e.g. Bolatto et al. 2013), and strong metallicity gradients have been found in some of the galaxies in this sample, as well as in larger samples of local star-forming galaxies (Ho et al. 2014; Chiang et al. 2018; Vílchez et al. 2019), reaching a factor of 10 within the optical radius. From an integrated perspective, instead, Genzel et al. (2015) find that α_{CO} varies little within $\pm$0.6 dex of the MS (thus for the large majority of the cells in this work). Nevertheless, such variations in metallicity need to be addressed properly in order to avoid biased interpretations of spatially resolved results. From the DustPedia archive, we download the table containing all the metallicity measurements available in literature (De Vis et al. 2019) and obtain in regions within R_{25} of the five galaxies in our sample. For NGC 5457, there are 280 estimates of metallicity within the optical radius, while for NGC 6946 only 14 are available. In particular, we make use of the metallicities computed exploiting the N2 and O3N2 calibrations of Pettini & Pagel (2004).[3] In particular, N2 is defined as $\log([N\,II_{6583A}/H_\alpha)$ and O3N2 as $\log[([O\,III]_{5007A}/H_\beta)/([N\,II]_{6583A}/H_\alpha)]$. With the conversion relations of Kewley, Geller & Jansen (2004), we obtain the metallicities in the Denicoló, Terlevich & Terlevich (2002) calibration. For each galaxy, we then build a 1D metallicity profile by fitting the different measurements. We use the 1D metallicity profile to obtain a 2D map of the metallicity dependent α_{CO} factor exploiting the relation of Genzel et al. (2012), that is obtained by fitting the $z \sim 0$ points of Leroy et al. (2011) with $z > 1$ ones collected in Genzel et al. (2012):

$$\log\alpha_{CO} = -1.3 \times (12 + \log(O/H))_{Denicolo02} + 12. \quad (5)$$

With the 2D map of $\log\alpha_{CO}$, we then estimate Σ_{H_2}. Fig. 5 shows a comparison of the molecular gas surface density computed considering a constant α_{CO} and the metallicity dependent one (in particular, the one obtained with the O3N2 calibration, but no significant differences are found when considering the N2 one). The highest scatter corresponds to small Σ_{H_2}, located in the outskirts of the optical disc, where the metallicity is, on average, smaller than in the centre. The source characterized by the largest scatter is NGC 5457, that is also the one with the strongest metallicity gradient (Vílchez et al. 2019). We note, nevertheless, that within 0.5 R_{25} (i.e. in first approximation, the distance within which the estimate of Σ_{H_2} is above the sensitivity limit), the maximum difference between the two estimates is around 0.2 dex.

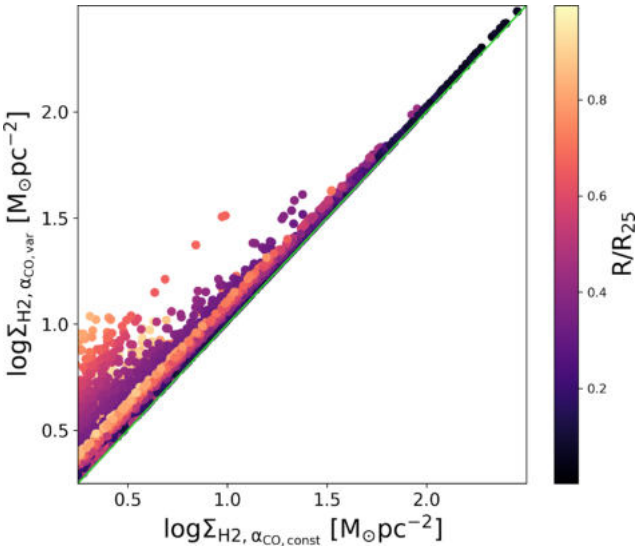

Figure 5. Comparison between the spatially resolved molecular gas mass computed with a constant α_{CO} factor and a metallicity dependent one (here for clarity we use the metallicity based on the O3N2 measurement; no significant differences are found when using the metallicity based on the N2 data). The points are colour coded as a function of their R/R_{25} value. The green solid line marks the 1-to-1 relation.

We repeat the previously shown analysis considering Σ_{H_2} estimated with the metallicity dependent α_{CO}. In Table 2, we report the slopes, intercepts, and scatter of the various relations discussed above: $\log\Sigma_{H_2}$–$\log\Sigma_{SFR}$, $\log\Sigma_{gas}$–$\log\Sigma_{SFR}$, $\log\Sigma_\star$–$\log\Sigma_{H_2}$, and $\log\Sigma_\star$–$\log\Sigma_{gas}$. With respect to the case of constant α_{CO}, the slope of molecular KS relation slightly increases but not significantly given the errors on the estimates. The slope of the total gas KS law decreases to reach values closer to 1, but again this decrease is not significant when taking the errors into account. Similarly, the variations in slope and intercept of the $\log\Sigma_\star$–$\log\Sigma_{H_2,gas}$ relations do not vary significantly with respect to the values found in Section 3.2. The scatter of the four relations slightly increases. In particular, the scatter of the $\log\Sigma_\star$–$\log\Sigma_{H_2,gas}$ relations is comparable or larger than the one of the spatially resolved MS. This is expected, as we are adding several sources of uncertainty: the conversion between different metallicity calibrations, the correlation between α_{CO} and metallicity, as well as the fact that we are averaging the metallicity to obtain a 1D profile. In first approximation, this exercise reveals that the results in this paper are robust against variations of the α_{CO} factor as a function of metallicity, that is the main and most studied dependence of α_{CO} on physical/galaxy properties (e.g. gas temperature and abundance, optical depth, cloud structure, cosmic ray density, and UV radiation field, in addition to the metallicity).

[3]We refer the reader to Casasola et al. (2020) and De Vis et al. (2019) for details of the metallicity calibration.

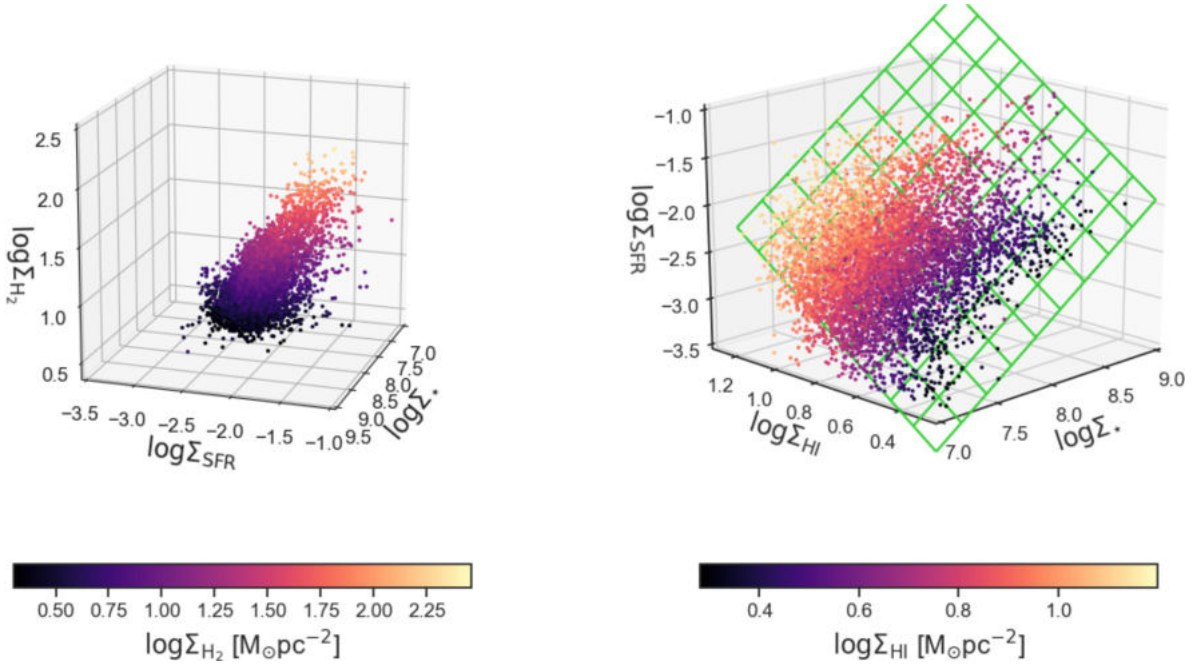

Figure 6. *Left-hand panel*: Distribution of the regions having an estimate of Σ_{H_2} above the sensitivity limit in the log $\Sigma_\star$–log Σ_{SFR} –log Σ_{H_2} plane. Each point is colour coded as a function of log Σ_{H_2}. Four projections of this space at different azimuthal angles are shown in Fig. A1. *Right-hand panel*: Distribution of the regions having an estimate of Σ_{HI} above the sensitivity limit in the log $\Sigma_\star$–log Σ_{SFR}–log Σ_{HI} plane. Each point is colour coded as a function of log Σ_{HI}. The best-fitting plane is indicated by the green grid. Four projections of this plane, described by equation (7), at different azimuthal angles are shown in Fig. A2.

This happens because the central metallicities for the galaxies in our sample are similar, and the molecular gas maps are not deep enough to reach the outermost regions where the metallicity decrease with respect to the central value.

4 DISCUSSION

4.1 The origin of the main sequence and its scatter

The spatially resolved MS of galaxies constitutes the building block of the integrated MS relation of star-forming galaxies, so deeply analysed in literature to understand the star formation processes and the quenching mechanisms. When analysing the molecular gas component of nearby galaxies we find tighter relations than the MS itself, and that may be at the physical origin of it: the KS law (2) and the MGMS (4). By combining equations (2) and (4), we obtain a spatially resolved MS in the form

$$\log \Sigma_{SFR} = 0.73 \times \log \Sigma_\star - 7.89, \quad (6)$$

which, as expected, consistent with the spatially resolved MS relation characterizing our sample (log Σ_{SFR} = 0.76log $\Sigma_\star$ − 8.15, see Section 2.1). We find that the Σ_{H_2}–Σ_{SFR} relation is the tightest one of the three, with a scatter of 0.19 dex, followed by the $\Sigma_\star$–Σ_{H_2} relation, 0.22 dex, similar to the scatter of the spatially resolved MS (0.23 dex). Contrary to Lin et al. (2019), we find that the scatter of the spatially resolved MS is significantly smaller than the quadratic sum of the scatters of the $\Sigma_\star$–Σ_{H_2} and Σ_{H_2}–Σ_{SFR} relations, indicating that the scatters of these relations are not independent. Indeed, regions located in the upper (lower) envelope of the molecular KS relation also populate the upper (lower) envelope of the MGMS. To further investigate the connection between the three relations (KS, MS, MGMS), we plot in the left-hand panel of Fig. 6 how regions with an estimate of Σ_{H_2} above the sensitivity limit populate the 3D space made by log $\Sigma_\star$, log Σ_{SFR}, and log Σ_{H_2} (four different projections of this space are shown in Fig. A1 in Appendix A). The variables define a 3D relation, as found by Lin et al. (2019). This is expected, as we find no dependence of Δ_{MS} on Σ_{H_2} (see Fig. 4). On the other hand, the analysis of Σ_{HI} in the log $\Sigma_\star$–log Σ_{SFR} plane revealed that the spatially resolved MS scatter seems to be connected to the presence of neutral gas. Indeed, when analysing how regions populate the 3D space formed by log $\Sigma_\star$, log Σ_{SFR}, and log Σ_{HI}, we find that they identify a plane, as shown in the right-hand panel of Fig. 6 (four different projections of this plane are shown in Fig. A2 in Appendix A). The equation of the plane that minimizes the perpendicular distance of the points can be written as

$$\log \Sigma_{SFR} = 0.97 \log \Sigma_\star + 1.99 \log \Sigma_{HI} - 11.11. \quad (7)$$

The relation expressed by equation (7) has a scatter of 0.14 dex, significantly smaller than the one of the spatially resolved MS relation. Interestingly, when the dependence of the SFR of H I surface densities is taken into account, the relation between log Σ_{SFR} and log $\Sigma_\star$ becomes closer to linear. To better understand the origin of the relation expressed by equation (7), in Fig. 7 we show the logΣ_{H_2}–logΣ_{HI} plane colour coded as a function of Δ_{MS} (left-hand panel) and r/R_{25} (right-hand panel). From Fig. 7, we can appreciate that regions with Σ_{HI} higher than 10 M⊙ pc^{-2} (that is the typical value for the H I to H2 transition, Bigiel et al. 2008; Leroy et al. 2008; Lee et al. 2012, 2014) correspond to the upper envelope of the spatially resolved MS and, on average, are preferentially located between 0.3 and 0.8 R_{25}. These regions span a wide range of logΣ_{H_2} values: (1) up to logΣ_{H_2} = 2 M$_\odot$ pc^{-2} for 0.3R_{25} < r <0.6 R_{25} and (2) below the sensitivity limit for r >0.6 R_{25}. In the first case, the stellar surface density and average SFR are moderately high: high H I surface densities could be partially due to H_2 dissociation and are needed (together with dust)

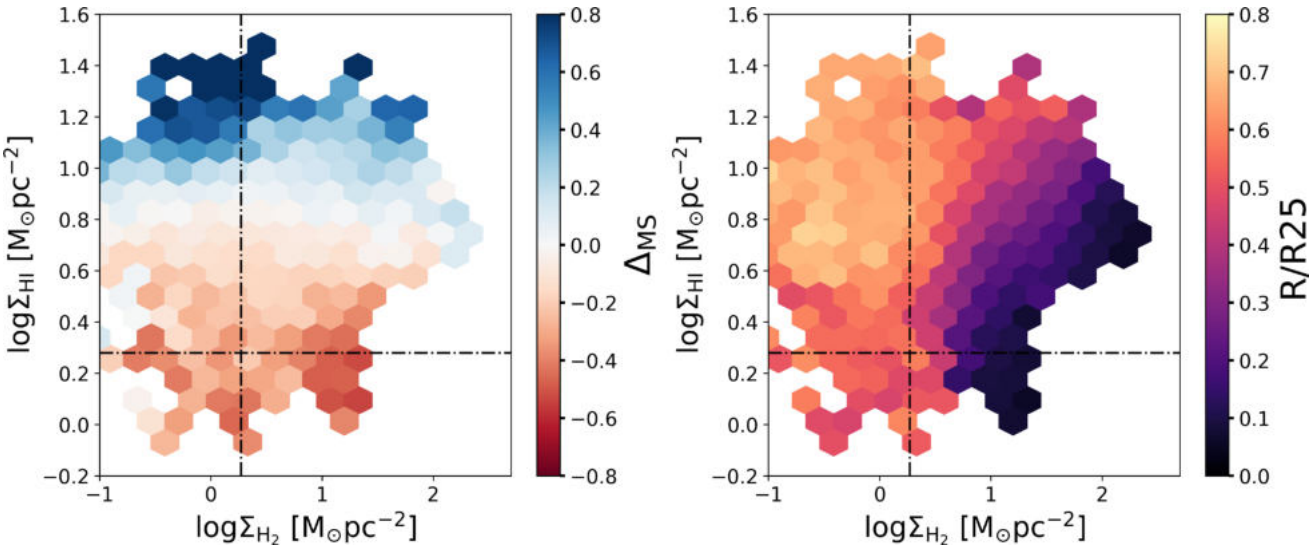

Figure 7. The $\log\Sigma_{H_2}$–$\log\Sigma_{HI}$ plane, colour coded as a function of Δ_{MS} (left-hand panel) and R/R_{25} (right-hand panel). Sensitivity limits are marked with dot–dashed lines.

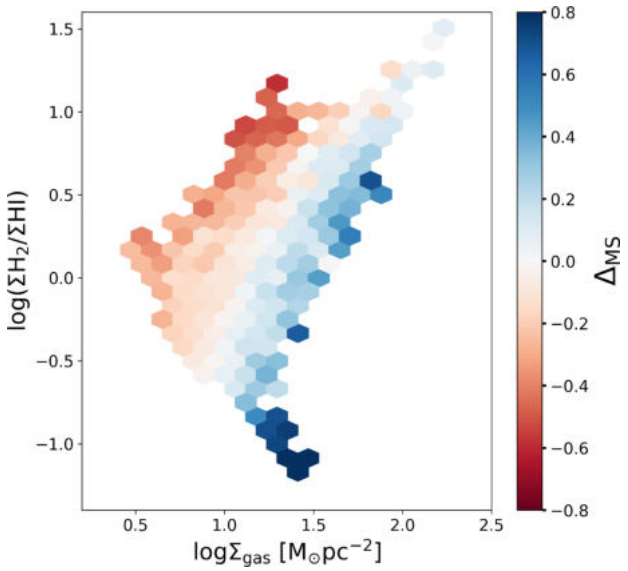

Figure 8. The Σ_{H_2}/Σ_{HI} ratio as a function of Σ_{gas}. The cells have been colour coded as a function of the average Δ_{MS}.

to prevent the further dissociation of the molecular gas by the intense radiation field. In the outer part of the optical disc, the SFRs are on average lower than in the inner disc, and so is the stellar surface density; nevertheless, the SFRs above the MS reach values that are comparable to SFRs on the MS in the inner part of the disc.

Most likely, once the molecular gas gives birth to new stars, it is partly disrupted by the resulting intense UV radiation from hot massive stars. To illustrate this effect, in Fig. 8, we plot the Σ_{H_2}/Σ_{HI} ratio as a function of Σ_{gas}. As expected, for higher Σ_{gas} this ratio increases: H_2 becomes progressively more dominant over H I as the chemical equilibrium shifts in favour of the molecular phase with increasing gas pressure. However, the correlation is quite broad, and the origin of the spread at fixed Σ_{gas} becomes evident once the cells are colour coded as a function of Δ_{MS}. Going from below to above the MS relation, Σ_{H_2}/Σ_{HI} steadily decreases. We interpret this trend as evidence that stellar feedback (radiative and from supernova shocks) has the effect of partially dissociating the H_2 molecules in regions of intense star formation. The sheer size of this trend is worth emphasizing, as the H_2/H I ratio drops by about a factor of 100 when going from extreme sub-MS to super-MS (starbursting) cells. Such a wide range is indeed expected by theory, for a wide variation of the intensity of the UV radiation field (cf. fig. 7 in Sternberg et al. 2014, see also Tacconi, Genzel & Sternberg 2020).

We notice that a correlation between the H I abundance and the distance from the MS has been recently reported by Wang et al. (2020) when analysing integrated galaxy properties; that is, galaxies above the MS are more H I-rich than those below. They interpret this trend in terms of H I being an intermediate step (between the ionized and the molecular phase) in fuelling star formation in galaxies, but do not consider H I as a product of molecular dissociation. Our results instead indicate that H I is also a product of star formation and its surface density is extremely sensitive to the local UV radiation field.

4.2 Star formation efficiency versus gas fraction

The data set in our hands gives us the possibility to analyse the role of SFE and f_{gas} in setting the sSFR of a region, thus deciding its location with respect to the spatially resolved MS relation. As in literature, the gas fraction and SFE estimates may or may not include the contribution of neutral gas, depending on how the gas mass is measured, we define the molecular, atomic, and total SFE: $SFE_{mol} = SFR/M_{H_2}$, $SFE_{ato} = SFR/M_{HI}$, $SFE_{tot} = SFR/(M_{HI}+M_{H_2})$. Similarly, we define the molecular, atomic and total gas fractions as $f_{gas,mol} = M_{H_2}/(M_{H_2}+M_{HI}+M_\star)$, $f_{gas,ato} = M_{HI}/(M_{H_2}+M_{HI}+M_\star)$ and $f_{gas,tot} = (M_{HI}+M_{H_2})/(M_{HI}+M_{H_2}+M_\star)$.

In Fig. 9, we show how the average SFE (top) and f_{gas} (bottom) vary in the $\log\Sigma_\star$–$\log\Sigma_{SFR}$ plane, separating the different phases. Qualitatively, we observe that SFE_{mol} varies strongly above and below the MS, for $\log\Sigma_\star < 8$ $M_\odot$ kpc^{-2}, while it is almost constant at higher stellar surface densities. These trends reflect the changes in $f_{gas,mol}$, that is characterized by strong variations above/below the MS only at higher stellar surface densities, leading to a constant SFE. We notice that regions above the MS at $\log\Sigma_\star < 7$ $M_\odot$ kpc^{-2} have very low $f_{gas,mol}$, as they are located in the outer optical disc. SFE_{ato} (central top panel) is nearly constant above/below the MS,

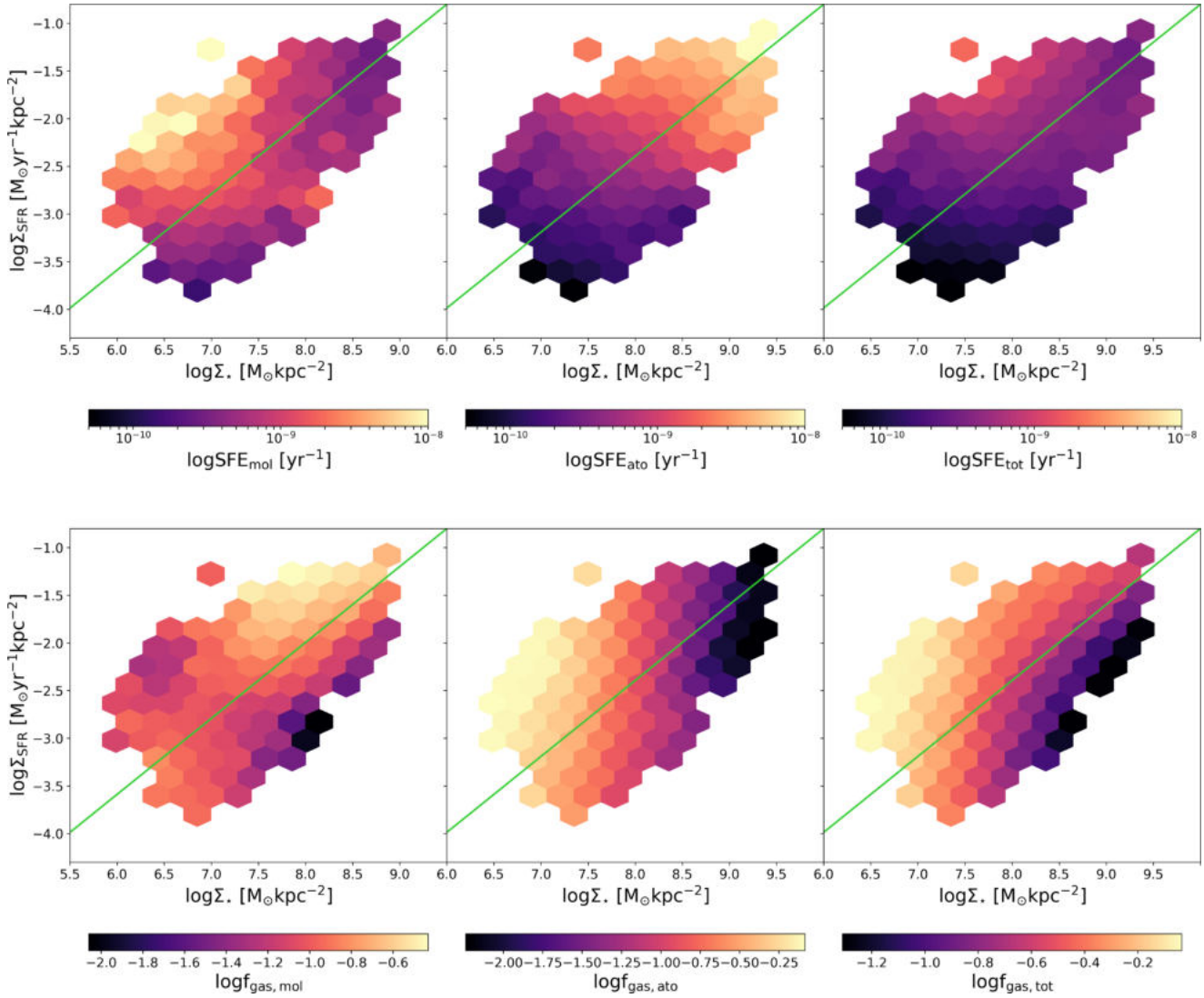

Figure 9. Molecular, atomic, and total SFE and $f_{\rm gas}$ in the $\log\Sigma_\star$–$\log\Sigma_{\rm SFR}$ plane. The bins in the six panels are colour coded as a function of $\rm SFE_{mol} = SFR/M_{H_2}$ in the *top left-hand panel*, $\rm SFE_{ato} = SFR/M_{H\,I}$ in the *top central panel*, $\rm SFE_{tot} = SFR/(M_{H\,I}+M_{H_2})$ in the *top right-hand panel*, $f_{\rm gas,mol} = M_{H_2}/(M_{H\,I}+M_{H_2}+M_\star)$ in the *bottom left-hand panel*, $f_{\rm gas,ato} = M_{H\,I}/(M_{H\,I}+M_{H_2}+M_\star)$ in the *bottom central panel*, and $f_{\rm gas,tot} = (M_{H\,I}+M_{H_2})/(M_{H\,I}+M_{H_2}+M_\star)$ in the *bottom right-hand panel*. The spatially resolved MS is indicated with the green solid line.

while it steadily increases along the MS relation for increasing stellar surface densities. The atomic gas fraction is subject to two distinct trends: it decreases along the MS relation, from low to high $\Sigma_\star$, and tends to be higher above the MS. When considering the total gas, the variations of $\rm SFE_{tot}$ are less evident: $\rm SFE_{tot}$ increases slightly at fixed stellar surface densities, less significantly in the direction perpendicular to the MS relation, and it increases along the MS for $\log\Sigma_\star < 7.5$ $\rm M_\odot$ $\rm kpc^{-2}$, to reach an almost constant value for $\log\Sigma_\star > 7.5$ $\rm M_\odot$ $\rm kpc^{-2}$. Finally, we observe that $f_{\rm gas,tot}$ varies strongly when moving from the lower to the upper envelope of the MS, both perpendicular to the relation and at fixed $\log\Sigma_\star$. Regions with $\log\Sigma_\star < 7.0\,\rm M_\odot$, that on average correspond to $\log\Sigma_{H_2}$ below the sensitivity limit, have large gas fractions thanks to the contribution of the neutral gas.

The qualitative analysis carried on so far on Fig. 9 points to the role of both the SFE and $f_{\rm gas}$ in regulating the SFR of a region. From an integrated point of view, there is now convergence on the fact that an increase in SFR at fixed $M_\star$ and cosmic epoch is due to a combination of increasing gas mass and decreasing depletion time (thus increasing SFE Saintonge et al. 2011b, 2012; Leroy et al. 2013; Huang & Kauffmann 2014). In the recent years, these studies could be carried out with larger and larger samples, using different sub-mm observations to trace gas, and exploring a wide range of cosmic epochs, $0 < z < 4.5$, with the general consensus that an almost equal increase of gas fraction and SFE can explain an increase in sSFR at fixed redshift. Scoville et al. (2017) exploited sub-mm ALMA continuum observations of 700 COSMOS galaxies at $0.3 < z < 4$ and estimated the gas mass from the dust mass. Several works in literature indicate that the dust mass is a tracer of the total gas mass (e.g. Leroy et al. 2011; Corbelli et al. 2012; Orellana et al. 2017; Casasola et al. 2020), but for $0.3 < z < 4$ the total gas is dominated by the molecular fraction (e.g. Lagos et al. 2014). Genzel et al. (2015) and Tacconi et al. (2018) combine three different estimates of molecular gas mass (from FIR SED, ∼1 mm dust photometry and CO line flux) in the redshift range $0 < z < 4$ and found that an increase in sSFR at fixed stellar mass and redshift is accompanied by an almost equal increase

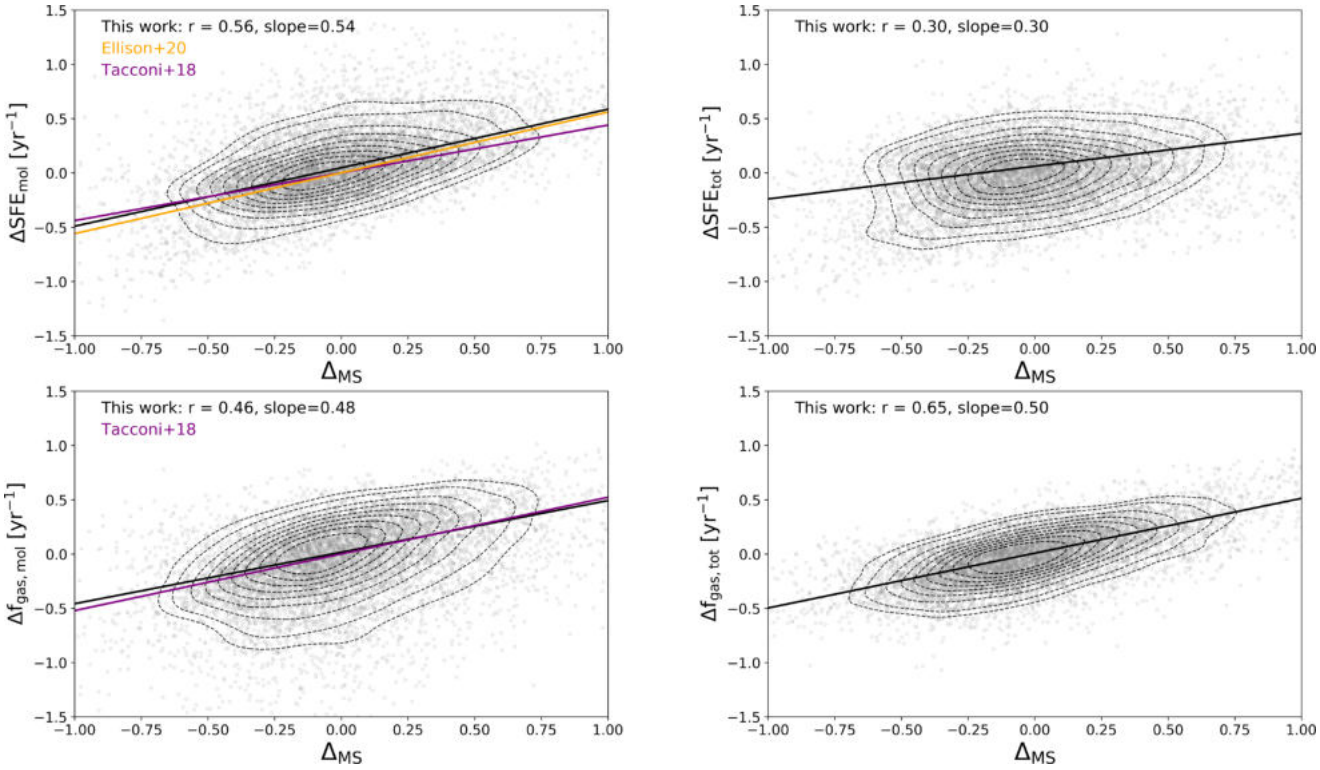

Figure 10. Distributions of regions in the $\Delta_{SFE,mol}$–Δ_{MS} plane (*top left-hand panel*), in the $\Delta_{SFE,tot}$–Δ_{MS} plane (*top right-hand panel*), $\Delta_{f_{gas,mol}}$ –Δ_{MS} plane (*bottom left-hand panel*), and $\Delta_{f_{gas,tot}}$–Δ_{MS} (*bottom right-hand panel*). The best-fitting relations of this work are shown as a black solid line. The best-fitting slope and the Pearson correlation coefficient are witting each panel. In the left-hand panels, we show relations of Tacconi et al. (2018) in purple, and the one of Ellison et al. (2020a) in orange.

of SFE and f_{gas}. Recently, Ellison et al. (2020b), using molecular gas observations from the ALMaQUEST survey (median redshift ∼0.03) on kpc scales, find that variations of the SFE play a major role in setting the SFR at fixed stellar mass (and thus the scatter of the spatially resolved MS), with differences in $f_{gas,mol}$ playing a secondary role. In Fig. 10, we compare our results to the trends found in Tacconi et al. (2018) and Ellison et al. (2020b). We define Δ_{SFE} as the distance of a region from the spatially resolved KS law at fixed molecular gas mass (central panel of Fig. 2), and $\Delta_{f_{gas}}$ as the distance of a region from the spatially resolved MGMS (central panel of Fig. 3), as done in Ellison et al. (2020b). As the analysis of the connection between the scatter of these relations and Δ_{MS} in Sections 3.2 and 3.1 revealed that MS regions are located along the KS and MGMS relations, the definitions of Δ_{SFE} and $\Delta_{f_{gas}}$ given above are consistent with those of Tacconi et al. (2018) that normalize t_{depl} and f_{gas} to their MS values. The panels show the variation between molecular and total SFE and gas fraction of a region with respect to the MS values (thus Δ_{SFE} and $\Delta_{f_{gas}}$) as a function of Δ_{MS}. The top left-hand panel shows the $\Delta_{SFE,mol}$–Δ_{MS} relation; the Pearson correlation coefficient is 0.56 and the best-fitting relation has a slope of 0.54 and a scatter of 0.18 dex, that is in excellent agreement with Tacconi et al. (2018, slope = 0.44) and Ellison et al. (2020b, slope = 0.5). We emphasize here that our work has a spatial resolution of 500 pc, thus reaching surface densities that are ∼1 dex smaller than Ellison et al. (2020b). A similar slope (0.48) is found when analysing $\Delta_{f_{gas,mol}}$ as a function of Δ_{MS}, with a Pearson coefficient of 0.47 and a scatter of 0.23 dex. Our best-fitting relation is in excellent agreement with the one of Tacconi et al. (2018) (obtained from integrated quantities) that has a slope of 0.52. These results emphasize that when analysing the molecular gas phase, an increase in SFR at fixed $M_\star$ and cosmic epoch is due to a combination of increasing gas mass and increasing (decreasing) SFE (t_{depl}). The situation painted by the molecular gas changes when the contribution of neutral gas is taken into account. In the left-hand panels of Fig. 10, we show the $\Delta_{SFE,tot}$–Δ_{MS} (top) and the $\Delta_{f_{gas,tot}}$–Δ_{MS} (bottom) planes, thus considering both the neutral and molecular gas phases. Interestingly, we see that the relation between $\Delta_{SFE,tot}$ and Δ_{MS} is significantly weaker than in the molecular case, as we retrieve a Pearson coefficient of 0.30, a slope of 0.30, and a scatter of 0.28 dex. On the other hand, we observe a stronger correlation between Δ_{MS} and $\Delta_{f_{gas,tot}}$ (Spearman ranking is 0.65), with a slope of 0.50 and a scatter of 0.19 dex. These results indicate the importance of the neutral gas phase in setting the scatter of the spatially resolved MS, as it partially traces molecular gas dissociated by the radiation field.

Finally, the data set in our hands allows us to analyse the spatial variations of SFE and f_{gas} within the five galaxies of the sample. The spatially resolved maps of Δ_{MS}, $\Delta_{SFE,tot}$, and $\Delta_{f_{gas,tot}}$ for every galaxy can be found in Appendix B (Figs B1 and B2). Here, we emphasize that while we do observe variations within galaxies and among them of the connection between Δ_{MS} and f_{gas} or SFE, on average the galaxy-by-galaxy analysis confirms that the gas fraction strongly correlates with Δ_{MS}.

5 CONCLUSIONS

In this manuscript, we exploit the combination of highly accurate measurements of $\Sigma_\star$ and Σ_{SFR} at 500 pc resolution of five nearby, face-on spiral galaxies obtained following the procedure presented in Paper I, with observations of neutral and molecular gas. With this powerful data set, we study how the location of a region with respect

to the spatially resolved main sequence (MS) is related to the gas in the different phases. We summarize here our main results:

(i) We find that $\log \Sigma_\star$, $\log \Sigma_{\rm SFR}$, and $\log \Sigma_{\rm H_2}$ define a 3D relation (the left-hand panel of Fig. 6); the three projections are the Kennicutt–Schmidt (KS) law, the MS, and the molecular gas main sequence (MGMS). The KS law is the tightest relation, with a scatter of 0.19 dex, followed by the MGMS (0.22 dex) and the spatially resolved MS (0.23 dex). The existence of the MGMS at sub-kpc scales opens up the possibility to study molecular gas content from $\log\Sigma_{\rm SFR}$ and $\log\Sigma_\star$ alone, which are generally easier to obtain and available for large samples.

(ii) We study the distribution of the neutral and molecular gas in the $\log\Sigma_\star$–$\log\Sigma_{\rm SFR}$ plane (Fig. 4) and we find that the surface density of molecular gas steadily increases along the MS relation, but is almost constant perpendicular to it. The surface density of neutral gas, instead, is almost constant along the MS, and increases (decreases) in its upper (lower) envelope. On average, regions located in the upper envelope of the spatially resolved MS have $\Sigma_{\rm H\,I} \geq 10\ {\rm M_\odot\ pc^{-2}}$, that is the typical value for the H I to H_2 transition. The three variables $\log \Sigma_\star$, $\log \Sigma_{\rm SFR}$, and $\log \Sigma_{\rm H\,I}$ are distributed along the plane $\log \Sigma_{\rm SFR} = 0.97 \log \Sigma_\star + 1.99 \log \Sigma_{\rm H\,I} - 11.11$ that has a scatter of 0.14 dex (the right-hand panel of Fig. 6).

(iii) When moving towards high $\Sigma_{\rm SFR}$ at fixed stellar surface densities, the molecular gas fraction and molecular SFE both increase. On the other hand, when we consider the total gas, thus also the contribution of the neutral component, we observe a steep increase of the gas fraction towards high SFRs, accompanied by a weak increase of the total SFE (Fig. 10).

Our results illustrate the intricate interplay between neutral and molecular gas, as it changes radially as a function of the distance from the centre of galaxies, as well as locally depending on the sSFR. We argue that molecular gas dissociation plays an important role in setting the observed trends of neutral and molecular gas surface densities around the MS relation (Fig. 8). Thus, high total gas surface densities favour the formation of molecular hydrogen clouds, which in turn promote star formation whose resulting UV radiation has the effect of dissociating the molecules, in a local baryon cycle that is a manifestation of the self-regulating nature of the star formation process. We shall return on these issues in a future paper, also expanding on their implications for our understanding of the star-formation process in high-redshift galaxies. These trends, obtained here for massive, disc-dominated spirals without a strong bar, will be analysed for galaxies with different morphologies (bulge dominated and spirals with strong bars) in another upcoming paper.

The continuity of trends above the MS, MGMS, and KS relations suggests that starburst regions do not result from a bi-modality in the star formation process, but rather from a steady variation of primarily the total gas fraction and partially the star formation efficiency. We speculate that this continuity could also explain the existence of high redshift starbursts, as the scatter of the spatially resolved MS is similar to the one of the integrated relation, and this last quantity is observed to be constant with redshift. It is widely believed that high-redshift galaxies are dominated by H_2 over H I, because their higher gas surface density favours the molecular phase. However, this finding suggests that the higher sSFR at high redshift may actually contrast this expectation, with intense stellar feedback leading to dissociation thus reducing the H_2/H I ratio. The next generation of radio telescopes like the $_{\rm Square}$ Kilometer Array (SKA), also ongoing surveys with MeerKAT, such as MIGHTEE (Jarvis et al. 2016) and LADUMA (Blyth et al. 2016), will directly measure the H I content in distant galaxies, thus unravelling its role in the star formation processes at earlier cosmic epochs.

ACKNOWLEDGEMENTS

We thank the anonymous referee for constructive comments that improved the manuscript. LM is grateful to Sara Ellison and Bhaskar Agarwal for helpful discussion on the manuscript. LM acknowledges support from the BIRD 2018 research grant from the ⟨0:funding-source 3:href="http://dx.doi.org/10.13039/501100003500"⟩Università degli Studi di Padova⟨/0:funding-source⟩. AE and GR are supported from the STARS@UniPD grant. GR acknowledges the support from grant PRIN MIUR 2017 – 20173ML3WW_001. GR and CM acknowledge funding from the INAF PRIN-SKA 2017 programme 1.05.01.88.04. We acknowledge funding from the INAF main stream 2018 programme 'Gas-DustPedia: A definitive view of the ISM in the Local Universe'. This research made use of PHOTUTILS, an ASTROPY package for detection and photometry of astronomical sources (Bradley et al. 2019).

DATA AVAILABILITY

This research is based on observations made with the Galaxy Evolution Explorer, obtained from the MAST data archive at the Space Telescope Science Institute, which is operated by the Association of Universities for Research in Astronomy, Inc., under NASA contract NASA 5-26555. This work made use of HERACLES, 'The HERACO-Line Extragalactic Survey' (Leroy et al. 2009), and THINGS, 'The H I Nearby Galaxy Survey' (Walter et al. 2008). DustPedia is a collaborative focused research project supported by the European Union under the Seventh Framework Programme (2007–2013) call (proposal no. 606847). The participating institutions are Cardiff University, UK; National Observatory of Athens, Greece; Ghent University, Belgium; Université Paris Sud, France; National Institute for Astrophysics, Italy and CEA (Paris), France. We acknowledge the usage of the HyperLeda database (http://leda.univ-lyon1.fr). The derived data underlying this article will be shared on reasonable request to the corresponding author.

REFERENCES

Abdurro'uf, Akiyama M., 2017, MNRAS, 469, 2806
Barrera-Ballesteros J. K. et al., 2020, MNRAS, 492, 2651
Bell E. F., Kennicutt Robert C. J., 2001, ApJ, 548, 681
Bigiel F., Leroy A., Walter F., Brinks E., de Blok W. J. G., Madore B., Thornley M. D., 2008, AJ, 136, 2846
Bigiel F., Leroy A., Walter F., Blitz L., Brinks E., de Blok W. J. G., Madore B., 2010, AJ, 140, 1194
Blitz L., Rosolowsky E., 2006, ApJ, 650, 933
Bluck A. F. L., Maiolino R., Sánchez S. F., Ellison S. L., Thorp M. D., Piotrowska J. M., Teimoorinia H., Bundy K. A., 2020, MNRAS, 492, 96
Blyth S. et al., 2016, in MeerKAT Science: On the Pathway to the SKA. p. 4
Boissier S., Prantzos N., Boselli A., Gavazzi G., 2003, MNRAS, 346, 1215
Bolatto A. D. et al., 2017, ApJ, 846, 159
Bolatto A. D., Wolfire M., Leroy A. K., 2013, ARA&A, 51, 207
Bouché N. et al., 2010, ApJ, 718, 1001
Bradley L. et al., 2019, astropy/photutils: v0.6
Brinchmann J., Charlot S., White S. D. M., Tremonti C., Kauffmann G., Heckman T., Brinkmann J., 2004, MNRAS, 351, 1151
Bundy K. et al., 2015, ApJ, 798, 7
Cano-Díaz M. et al., 2016, ApJ, 821, L26
Cano-Díaz M., Ávila-Reese V., Sánchez S. F., Hernández-Toledo H. M., Rodríguez-Puebla A., Boquien M., Ibarra-Medel H., 2019, MNRAS, 488, 3929
Casasola V. et al., 2017, A&A, 605, A18
Casasola V. et al., 2020, A&A, 633, A100
Casasola V., Hunt L., Combes F., García-Burillo S., 2015, A&A, 577, A135
Chabrier G., 2003, PASP, 115, 763

Chiang I. D., Sandstrom K. M., Chastenet J., Johnson L. C., Leroy A. K., Utomo D., 2018, ApJ, 865, 117
Clark C. J. R. et al., 2018, A&A, 609, A37
Corbelli E. et al., 2012, A&A, 542, A32
Corbelli E. et al., 2017, A&A, 601, A146
da Cunha E., Charlot S., Elbaz D., 2008, MNRAS, 388, 1595
Daddi E. et al., 2007, ApJ, 670, 156
Daddi E. et al., 2010, ApJ, 714, L118
Davies J. I. et al., 2017, PASP, 129, 044102
de los Reyes M. A. C., Kennicutt Robert C. J., 2019, ApJ, 872, 16
De Vis P. et al., 2019, A&A, 623, A5
Dekel A. et al., 2009, Nature, 457, 451
Denicoló G., Terlevich R., Terlevich E., 2002, MNRAS, 330, 69
Dey B. et al., 2019, MNRAS, 488, 1926
Elbaz D. et al., 2007, A&A, 468, 33
Ellison S. L., Thorp M. D., Pan H.-A., Lin L., Scudder J. M., Bluck A. F. L., Sánchez S. F., Sargent M., 2020a, MNRAS, 492, 6027
Ellison S. L. et al., 2020b, MNRAS, 493, L39
Elmegreen B. G., 1993, ApJ, 411, 170
Enia A. et al., 2020, MNRAS, 493, 4107 (Paper I)
Ford G. P. et al., 2013, ApJ, 769, 55
Foreman-Mackey D., Hogg D. W., Lang D., Goodman J., 2013, PASP, 125, 306
Freundlich J. et al., 2013, A&A, 553, A130
Freundlich J. et al., 2019, A&A, 622, A105
Genzel R. et al., 2010, MNRAS, 407, 2091
Genzel R. et al., 2011, ApJ, 733, 101
Genzel R. et al., 2012, ApJ, 746, 69
Genzel R. et al., 2013, ApJ, 773, 68
Genzel R. et al., 2015, ApJ, 800, 20
Hall C., Courteau S., Jarrett T., Cluver M., Meurer G., Carignan C., Audcent-Ross F., 2018, ApJ, 865, 154
Ho I. T. et al., 2014, MNRAS, 444, 3894
Hopkins P. F., Kereš D., Oñorbe J., Faucher-Giguère C.-A., Quataert E., Murray N., Bullock J. S., 2014, MNRAS, 445, 581
Hsieh B. C. et al., 2017, ApJ, 851, L24
Huang M.-L., Kauffmann G., 2014, MNRAS, 443, 1329
Jarvis M. et al., 2016, in Proceedings of MeerKAT Science: On the Pathway to the SKA. 25-27 May, 2016 Stellenbosch, South Africa (MeerKAT2016). p. 6, Online at: https://pos.sissa.it/cgi-bin/reader/conf.cgi?confid=277
Kashino D. et al., 2013, ApJ, 777, L8
Kennicutt Robert C. J., 1998, ApJ, 498, 541
Kennicutt R. C., Evans N. J., 2012, ARA&A, 50, 531
Kewley L. J., Geller M. J., Jansen R. A., 2004, AJ, 127, 2002
Kruijssen J. M. D. et al., 2019, Nature, 569, 519
Krumholz M. R., McKee C. F., 2005, ApJ, 630, 250
Krumholz M. R., Dekel A., McKee C. F., 2012, ApJ, 745, 69
Kumari N., Irwin M. J., James B. L., 2020, A&A, 634, A24
Kurczynski P. et al., 2016, ApJ, 820, L1
Lagos C. d. P., Davis T. A., Lacey C. G., Zwaan M. A., Baugh C. M., Gonzalez-Perez V., Padilla N. D., 2014, MNRAS, 443, 1002
Lee N. et al., 2017, MNRAS, 471, 2124
Lee M.-Y. et al., 2012, ApJ, 748, 75
Lee M.-Y., Stanimirović S., Wolfire M. G., Shetty R., Glover S. C. O., Molina F. Z., Klessen R. S., 2014, ApJ, 784, 80
Leroy A. K. et al., 2009, AJ, 137, 4670
Leroy A. K. et al., 2011, ApJ, 737, 12
Leroy A. K. et al., 2013, AJ, 146, 19
Leroy A. K., Walter F., Brinks E., Bigiel F., de Blok W. J. G., Madore B., Thornley M. D., 2008, AJ, 136, 2782
Lilly S. J., Carollo C. M., Pipino A., Renzini A., Peng Y., 2013, ApJ, 772, 119
Lin L. et al., 2017, ApJ, 851, 18
Lin L. et al., 2019, ApJ, 884, L33
Makarov D., Prugniel P., Terekhova N., Courtois H., Vauglin I., 2014, A&A, 570, A13
Medling A. M. et al., 2018, MNRAS, 475, 5194
Mihos J. C., Harding P., Spengler C. E., Rudick C. S., Feldmeier J. J., 2013, ApJ, 762, 82
Morselli L., Popesso P., Cibinel A., Oesch P. A., Montes M., Atek H., Illingworth G. D., Holden B., 2019, A&A, 626, A61
Noeske K. G. et al., 2007, ApJ, 660, L47
Orellana G. et al., 2017, A&A, 602, A68
Orr M. E. et al., 2018, MNRAS, 478, 3653
Pearson W. J. et al., 2018, A&A, 615, A146
Peng Y.-j., Renzini A., 2020, MNRAS, 491, L51
Pettini M., Pagel B. E. J., 2004, MNRAS, 348, L59
Planck Collaboration XIII, 2016, A&A, 594, A13
Popesso P. et al., 2019, MNRAS, 483, 3213
Rodighiero G. et al., 2011, ApJ, 739, L40
Roychowdhury S., Huang M.-L., Kauffmann G., Wang J., Chengalur J. N., 2015, MNRAS, 449, 3700
Saintonge A. et al., 2011a, MNRAS, 415, 32
Saintonge A. et al., 2011b, MNRAS, 415, 61
Saintonge A. et al., 2012, ApJ, 758, 73
Salim S. et al., 2007, ApJS, 173, 267
Santini P. et al., 2017, ApJ, 847, 76
Schmidt M., 1959, ApJ, 129, 243
Schreiber C. et al., 2015, A&A, 575, A74
Schruba A. et al., 2011, AJ, 142, 37
Scoville N. et al., 2017, ApJ, 837, 150
Shetty R., Kelly B. C., Bigiel F., 2013, MNRAS, 430, 288
Shetty R., Kelly B. C., Rahman N., Bigiel F., Bolatto A. D., Clark P. C., Klessen R. S., Konstandin L. K., 2014a, MNRAS, 437, L61
Shetty R., Clark P. C., Klessen R. S., 2014b, MNRAS, 442, 2208
Shi Y. et al., 2018, ApJ, 853, 149
Shi Y., Helou G., Yan L., Armus L., Wu Y., Papovich C., Stierwalt S., 2011, ApJ, 733, 87
Silverman J. D. et al., 2015, ApJ, 812, L23
Silverman J. D. et al., 2018, ApJ, 867, 92
Solomon P. M., Downes D., Radford S. J. E., Barrett J. W., 1997, ApJ, 478, 144
Speagle J. S., Steinhardt C. L., Capak P. L., Silverman J. D., 2014, The Astrophysical Journal Supplement Series, 214, 15
Springel V., Hernquist L., 2003, MNRAS, 339, 312
Sternberg A., Le Petit F., Roueff E., Le Bourlot J., 2014, ApJ, 790, 10
Swaters R. A., van Albada T. S., van der Hulst J. M., Sancisi R., 2002, A&A, 390, 829
Tacchella S., Dekel A., Carollo C. M., Ceverino D., DeGraf C., Lapiner S., Mand elker N., Primack Joel R., 2016, MNRAS, 457, 2790
Tacconi L. J. et al., 2010, Nature, 463, 781
Tacconi L. J. et al., 2013, ApJ, 768, 74
Tacconi L. J. et al., 2018, ApJ, 853, 179
Tacconi L. J., Genzel R., Sternberg A., 2020, preprint (arXiv:2003.06245)
Tan J. C., 2000, ApJ, 536, 173
Vílchez J. M., Relaño M., Kennicutt R., De Looze I., Mollá M., Galametz M., 2019, MNRAS, 483, 4968
Vulcani B. et al., 2019, MNRAS, 488, 1597
Walter F., Brinks E., de Blok W. J. G., Bigiel F., Kennicutt Robert C. J., Thornley M. D., Leroy A., 2008, AJ, 136, 2563
Wang J. et al., 2013, MNRAS, 433, 270
Wang J., Catinella B., Saintonge A., Pan Z., Serra P., Shao L., 2020, ApJ, 890, 63
Whitaker K. E., van Dokkum P. G., Brammer G., Franx M., 2012, ApJ, 754, L29
Wyder T. K. et al., 2009, ApJ, 696, 1834

SUPPORTING INFORMATION

Supplementary data are available at *MNRAS* online.

FigureA1_animated.mp4
FigureA2_animated.mp4

Please note: Oxford University Press is not responsible for the content or functionality of any supporting materials supplied by the authors. Any queries (other than missing material) should be directed to the corresponding author for the article.

APPENDIX A: THE LOG $\Sigma_\star$–LOG Σ_{SFR}–log $\Sigma_{H_2,HI}$ 3D RELATION

As shown in Fig. 6, the three quantities log $\Sigma_\star$, log Σ_{SFR}, and log Σ_{H_2} define a 3D relation. To better visualize this relation, in Fig. A1 we show four different projections of it, corresponding to azimuthal angles of 0°, 60°, 120°, and 180°. We stress here that we are plotting only the regions that have an estimate of Σ_{H_2} above the sensitivity limit. In Fig. A2, we show, instead, the log $\Sigma_\star$, log Σ_{SFR}, and log Σ_{HI} 3D plane at four different azimuthal angles, with the aim of better visualize the positioning of the cells along the 3D plane marked in green. We plot in Fig. A2 only the regions that have an estimate of Σ_{HI} above the sensitivity limit.

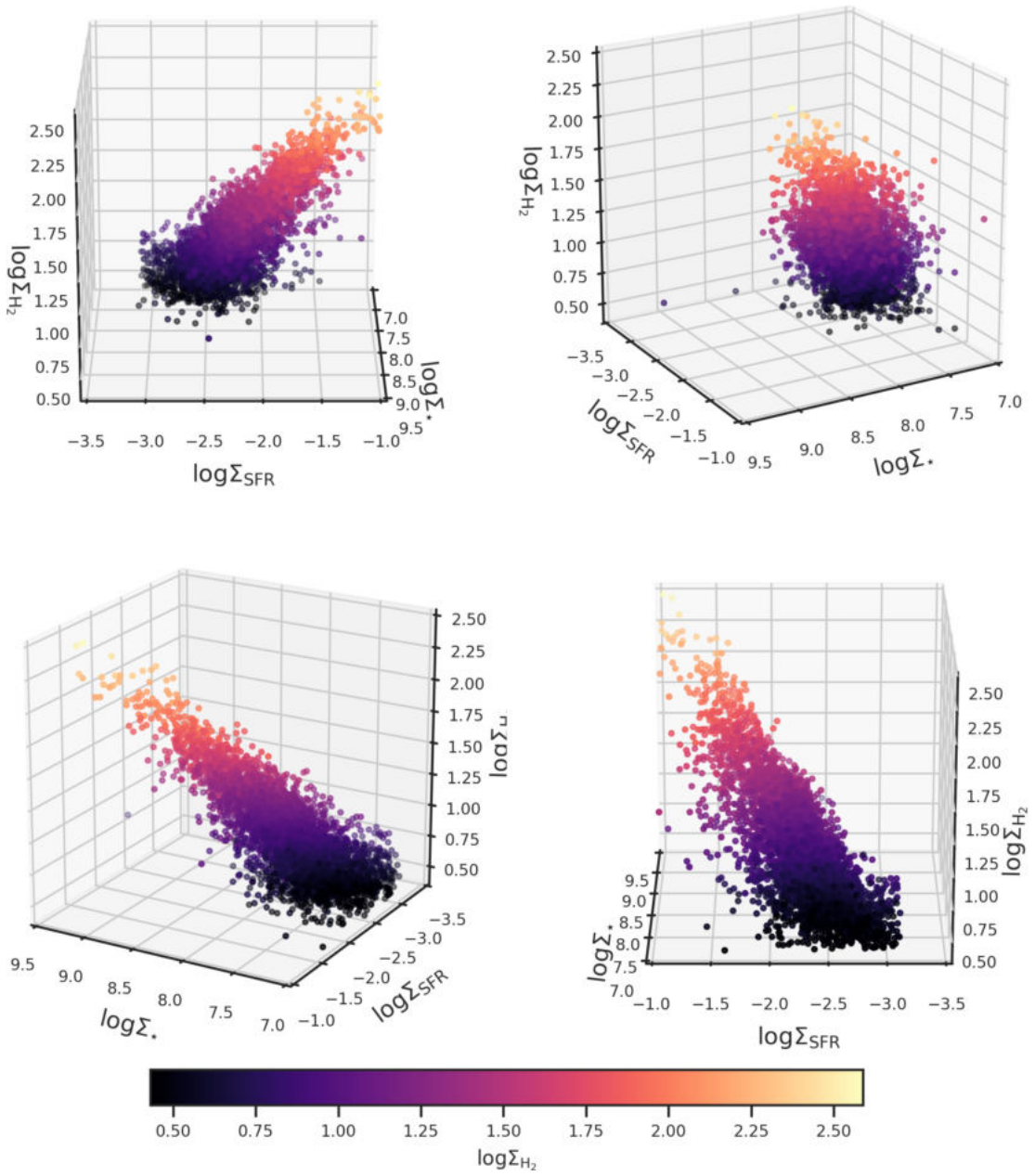

Figure A1. Distribution of the regions with an estimate of log Σ_{H_2} above the sensitivity limit in the log $\Sigma_\star$–log Σ_{SFR}–log Σ_{H_2} 3D space. For different projections of the plane are shown, corresponding to different azimuthal angles: 0° (top left), 60° (top right), 120° (bottom left), and 180 ° (bottom right). The point are colour coded as a function of log Σ_{HI}.

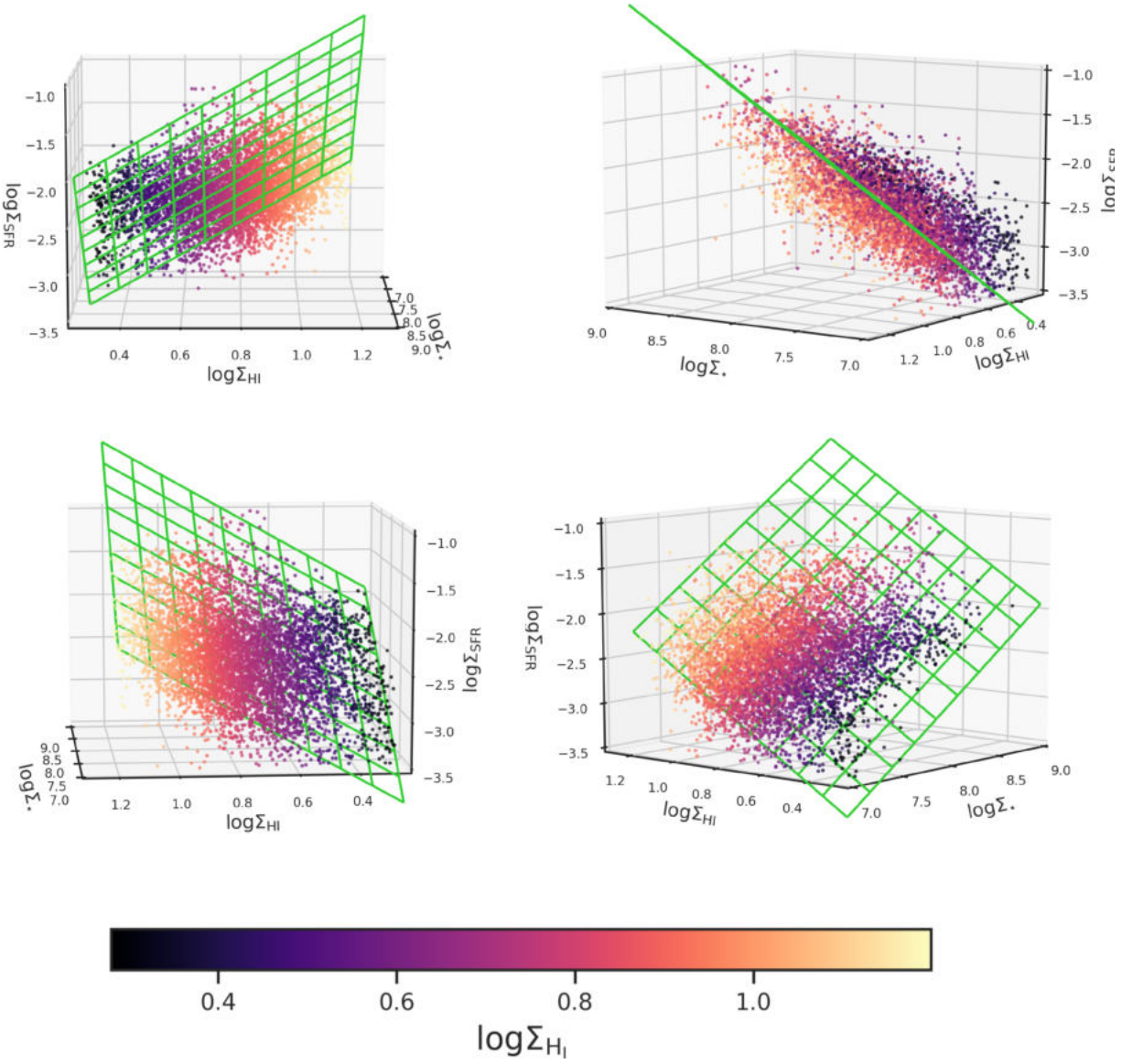

Figure A2. Distribution of the regions with an estimate of log $\Sigma_{\rm H\,I}$ above the sensitivity limit in the log $\Sigma_\star$–log $\Sigma_{\rm SFR}$–log $\Sigma_{\rm H_I}$ 3D space. For different projections of the plane are shown, corresponding to different azimuthal angles: 0° (top left), 125° (top right), 175° (bottom left), and 220 ° (bottom right). The points are colour coded as a function of log $\Sigma_{\rm H_2}$.

APPENDIX B: $\Delta_{\rm MS}$, SFE, AND GAS CONTENT WITHIN GALAXIES

In this section, we discuss the distributions of $\Delta_{\rm MS}$, $\Delta_{\rm f_{gas,tot}}$, and $\Delta_{\rm SFE,tot}$ within the five galaxies in our sample, shown in Figs B1 and B2. We recall here that $\Delta_{\rm SFE,tot}$ and $\Delta_{\rm f_{gas,tot}}$ are computed as the distance of the region from the global total gas–SFR relation (the right-hand panel of Fig. 2) and from the global total gas–mass relation (the right-hand panel of Fig. 3), and are thus a measure of the SFE and gas content with respect to the value on the best-fitted relation at a given gas or stellar surface density (e.g. regions with $\Delta_{\rm f_{gas,tot}} > 0$ have higher gas content than the average).

It is clear that the $\Delta_{\rm SFE,tot}$ and the $\Delta_{\rm f_{gas,tot}}$ in the inner regions will be anticorrelated because the regions where the bulk of molecular hydrogen is not spatially coincident with the regions where the FUV star formation tracer peaks. This is due to the time-delay between the formation of molecular clouds and the exposed phase of star formation (Corbelli et al. 2017). In the inner regions of spiral galaxies, the spiral pattern rotates slower than the stars and hence molecular clouds form out of compressed gas along the inner part of the arm. These are the regions with higher gas fraction than the average. The young stars become visible after dispersing the original gas and, moving faster than the arm, they appear shifted with respect to the newly formed molecular complexes. These are regions with low gas content but numerous visible young stars, hence appear with a star formation efficiency above the average. For the outer regions, at or beyond corotation, the situation should reverse with respect to the arm but the anticorrelation between $\Delta_{\rm SFE,tot}$ and the $\Delta_{\rm f_{gas,tot}}$ should still hold. Here, the low surface density of molecules and the presence of external perturbations make the study more challenging: tidal perturbations, gas stripping, and infall have a strong impact and this reflects on $\Delta_{\rm MS}$ that can vary substantially from one region to the next, being star-forming regions more coarsely spaced in the outer

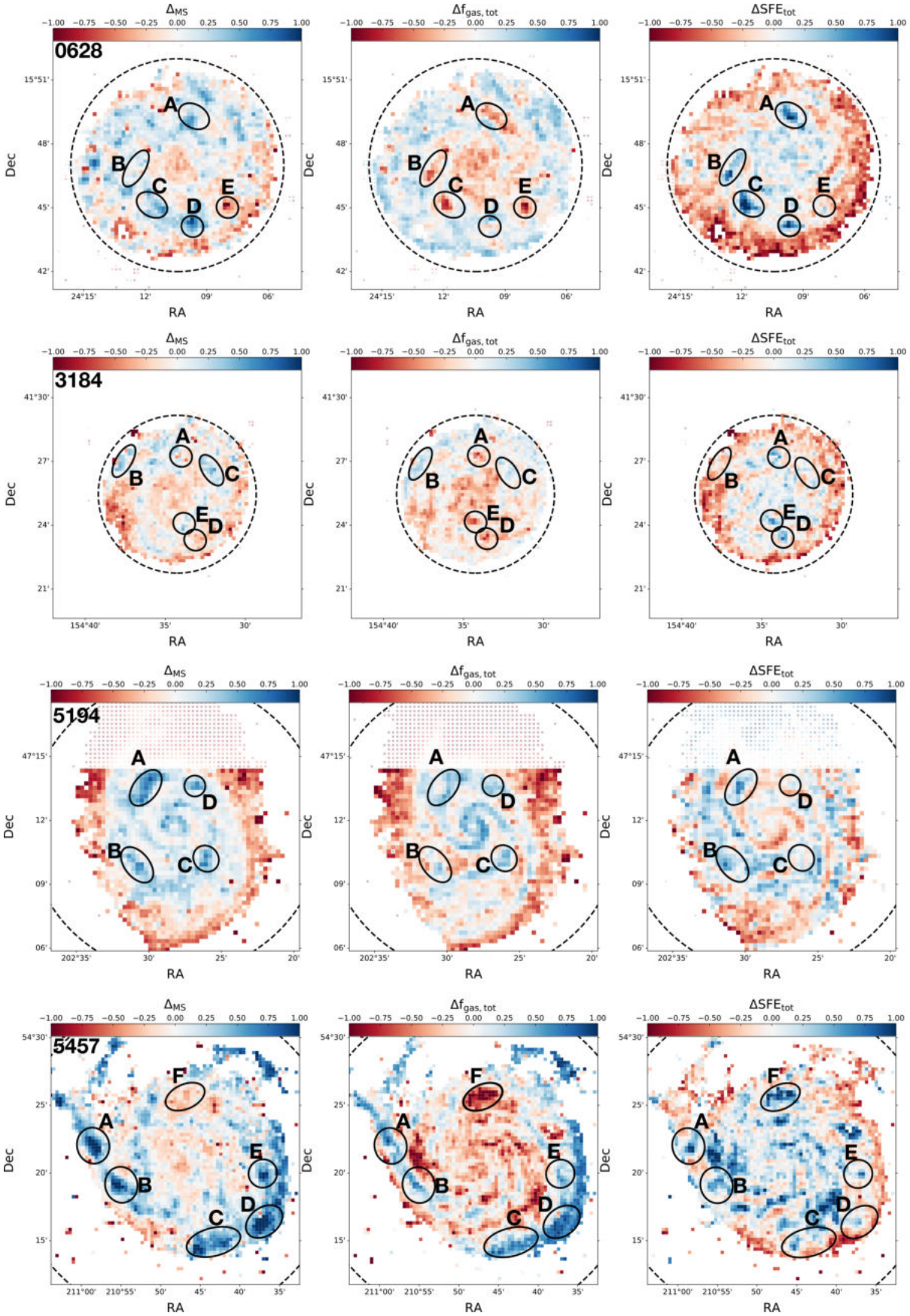

Figure B1. Δ_{MS} (left), $\Delta_{f_{gas,tot}}$ (centre), and $\Delta_{SFE,tot}$ (right) maps of (from top to bottom) NGC 0628, NGC 3184, NGC 5194, and NGC 5457. The highlighted regions are discussed more in detail in the text.

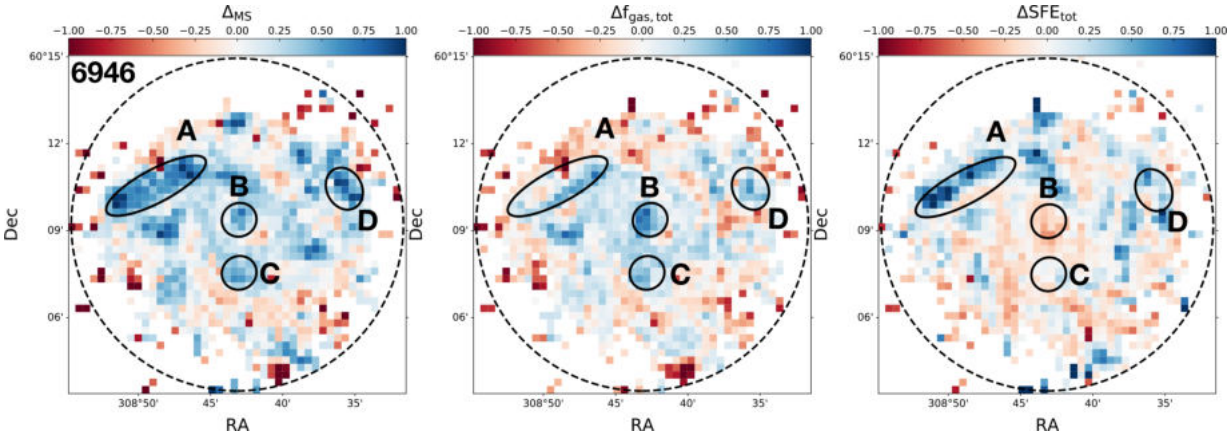

Figure B2. Δ_{MS} (left), $\Delta_{f_{gas,tot}}$ (centre), and $\Delta_{SFE,tot}$ (right) maps of NGC 6946. The highlighted regions are discussed more in detail in the text.

discs. Below we describe a few selected regions in each galaxy more in detail:

(i) The central region of NGC 0628, i.e. the bulge, is located below the MS and has low gas content, while $\Delta_{SFE,tot}$ varies of ± 0.3 dex around zero. Regions located in the upper envelope of the MS relation are located mostly along the spiral arms. We observe regions where $\Delta_{MS} \sim 0$ (A, B, and C) or $\Delta_{MS} \sim 1$ (D), or $\Delta_{MS} \sim -1$ (E), all with low gas fractions and high or average SFE.

(ii) NGC 3184 also has a central region characterized by mostly negative Δ_{MS} and $\Delta_{f_{gas,tot}}$, while $\Delta_{SFE,tot}$ is, for the majority of cells, positive. In the spiral arms, we observe regions where the SFR is significantly higher than the MS value (B and C) that correspond to gas fractions above the average, and varying SFE. We identify three blobs (A, D, and E) with negative $\Delta_{f_{gas,tot}}$ and Δ_{MS} varying slightly around the MS value (as in A and E) or $\Delta_{MS} < 0$ (as in D).

(iii) NGC 5194 is characterized by a central region that has SFR values mostly above the MS. Positive values of Δ_{MS} are located mainly along the spiral arms that are also well traced by an excess of total gas compared to the average. The regions A, B, C, and D are all above the MS relation, but they show different properties: while the majority of pixels within C and D are have $\Delta_{f_{gas,tot}} > 0$ and $\Delta_{SFE,tot} \sim 0$, A and B show clumps of $\Delta_{SFE,tot}$ well above 0 and $\Delta_{f_{gas,tot}}$ varying between negative and positive values.

(iv) NGC 5457 is characterized by two strong spiral arms with several blobs that have an SFR higher than the MS value (regions A, B, C, D, E). Within these regions, we observe gas fractions that are almost always higher than the MS values, while $\Delta_{SFE,tot}$ varies more strongly between positive and negative values. Region F, for which the majority of cells are well below the MS relation, has $\Delta_{SFE,tot} \sim 1$, but $\Delta_{f_{gas,tot}} \sim -1$.

(v) NGC 6946 has a central region characterized by SFR higher than MS values, high gas content and SFE lower than the average (region B). Regions A, C, and D are also characterized by values of Δ_{MS} close to 1, but different SFE. While regions A and D have close to normal gas content and SFE above the average, the more central regions B and C have a high gas content but a low SFE.

In general, we conclude that in the innermost and outer regions the decrease or enhancement of the local gas content follows closely that of the star formation rate along the MS. For the innermost region and the spiral arms, the enhancement or decrease of the SFE is opposite to that of the local gas content. But there are exceptions to this behaviour. Given the possible temporal and spatial lag between molecular and FUV peaks (Kruijssen et al. 2019), the relation between $\Delta_{SFE,tot}$ and Δ_{MS} for individual galaxies is more complex and requires dedicated analysis.

This paper has been typeset from a TEX/LATEX file prepared by the author.